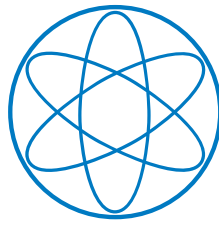Antonia Frank

Impact of the Plasma Curvature and the Probing Beam Geometry on Doppler Reflectometer Velocity Measurements

Master Thesis in Physics at
Technische Universität München

Impact of the Plasma Curvature and the Probing Beam Geometry on Doppler Reflectometer Velocity Measurements

presented by

Antonia Frank

October 6th 2021

First Promoter: Prof. Dr. Ulrich Stroth

Second Promoter: Dr. Philipp Lauber

Supervisor: Dr. Tim Happel

Abstract

The quality of confinement in magnetically confined fusion plasmas can be significantly deteriorated by turbulent transport. This makes a comprehensive understanding of turbulence in plasmas essential. Since radially sheared poloidal plasma flows can reduce turbulence and thereby transport, they are a relevant input parameter for predictive simulations of turbulent transport.

Doppler reflectometry is a diagnostic technique that can be used to study turbulence in fusion plasmas. It is a microwave diagnostic that exploits the back-scattering of electromagnetic waves from turbulent structures to obtain localized information about the perpendicular wavenumber spectrum of turbulence, the perpendicular propagation velocity of density fluctuations and the radial electric field for a wide range of spatially accessible regions.

In the recent past, poloidal asymmetries in the perpendicular velocity measurement have been observed in various fusion devices using Doppler reflectometry. An explanation of these asymmetries may lie in the diagnostic response.

Hence, numerical investigation using synthetic diagnostics is of great interest. The IPF-FD3D full-wave code is used as a synthetic Doppler reflectometry diagnostic, simulating microwave propagation and plasma-wave interaction at the cut-off layers in the plasma. The velocity measurement is studied in slab geometry and circular geometry using both isotropic and anisotropic synthetic turbulence. In particular, the analyses focus on the effects of various turbulence levels, the turbulence wavenumber spectrum, the poloidal position of the measurement antenna, and anisotropic turbulence structures.

Furthermore, the impact of the density wavenumber spectrum on the measurement of the perpendicular velocity is studied analytically. Doppler reflectometry probes the perpendicular wavenumber spectrum with a spectral resolution $\Delta k_\perp$ around a central $k_\perp$. Depending on the underlying density wavenumber spectrum, this spectral width can have a decisive influence on the measured velocities. An analytical expression for predicting the deviations due to this diagnostic effect is derived and used for comparison with the results from full-wave simulations.

Good agreement between analytical predictions and full-wave simulation results is obtained for all plasma geometries and types of synthetic turbulence. No other deviations are observed in the study. The magnitude of the observed diagnostic effect depends strongly on the geometry of the measurement beam and the plasma curvature and has to be considered under certain experimental conditions. However, the identified diagnostic effect is less pronounced than the poloidal asymmetries measured some the experiments, which could point to a real physics effect.

Contents

Contents

Bibliography 57

1 Introduction

Since the 1950s scientist have been trying to investigate the magnetic confinement of high-temperature plasmas with the purpose to build a fusion reactor [1].

Plasma is a gas of charged particles that forms at high temperatures through ionisation processes. Since it is in contrast to neutral gas, it is often referred to as the fourth state of matter. Due to the electric charge this state is characterized by strong collective effects and high conductivity. Under sufficiently high energies (keV range) due to high temperature or pressure, particles with light nuclei can overcome the Coulomb barrier and fuse to form a heavier nucleus. This releases energy, corresponding to the mass defect between product and reactants. These fusion processes are constantly ongoing in the universe, such as in stars. However, this principle is also used to develop a source of energy in form of a fusion reactor on the Earth.

Therefore, the reaction between deuterium (D) an tritium (T) seems to be the most likely because of the high fusion cross-section and the large energy release. The nuclei fuse into helium (He) and a neutron, which carries most of the energy.

$$\mathrm{D} + \mathrm{T} \rightarrow {}^4\mathrm{He}\,(3.5\,\mathrm{MeV}) + \mathrm{n}\,(14.1\,\mathrm{MeV}). \tag{1.1}$$
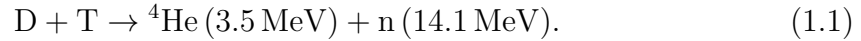
To enable fusion, particle diffusion must be counteracted by a confining force. While in stars gravity undertakes this function, for nuclear fusion on Earth the plasma can be kept together by magnetic confinement. The charged particles are bound to the magnetic field lines via gyromotion due to the Lorentz force.

An overall measure for the quality of confinement is the so-called energy confinement time τ_E. This time is one of the main parameters in the so-called triple product [2]

$$nT\tau_E > 3 \cdot 10^{21} \mathrm{keVs/m}^3, \tag{1.2}$$

where n is the density and T the temperature. It provides a minimum estimate to achieve reactor conditions with fusion. When the condition (1.2) is satisfied, ignition occurs and the fusion reaction becomes self-sustaining.

The tokamak, whose sketch is shown in figure 1.1(a), is an axisymmetric magnetic confinement device. The confining magnetic field is a combination of a toroidal field B_t generated by external poloidal coils and a poloidally revolving field B_θ. The latter is induced by a toroidal plasma current generated by transformer coils at the torus center. Additional stability is obtained using vertical field coils. The magnetic field forms torus shaped nested magnetic flux surfaces and thus inhibit to large degree particle and energy losses. The magnetic flux surfaces are usually designated by the
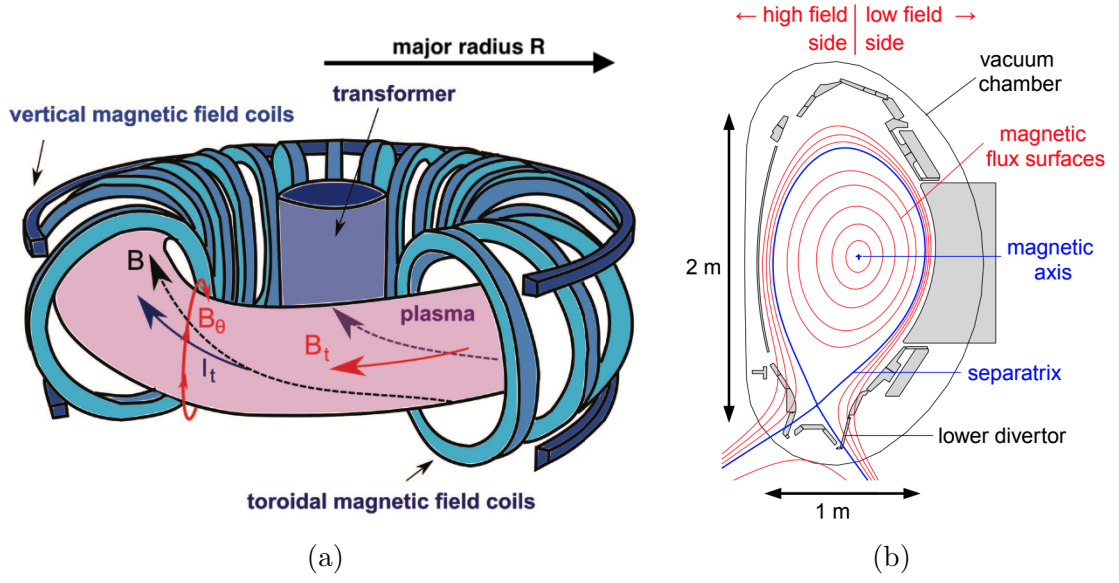
Figure 1.1: (a) Sketch of a tokamak (adapted form [4]) and (b) poloidal cross-section of ASDEX Upgrade (adapted form [5]).

normalized poloidal radius ρ_{pol}, which is defined by

$$\rho_{pol} = \sqrt{\frac{\Psi - \Psi_0}{\Psi_S - \Psi_0}}. \tag{1.3}$$

where Ψ_0 is the poloidal magnetic flux on the magnetic axis at the center of the plasma and Ψ_S is the magnetic flux on the separatrix, which is the last closed flux surface. It therefore varies from 0 at the plasma center to 1 at the plasma edge. The flux surfaces and associated parameters are shown in figure 1.1(b).

This cross-section is related to the experimental device AxialSymmetric Divertor EXperiment *ASDEX Upgrade* (AUG) [3]. This medium size tokamak located at the Max Planck Institute in Garching, Germany, is used as a reference in this work. The machine has a D-shaped poloidal cross-section and is is equipped with a divertor, which diverts the magnetic field at the plasma edge towards collector plates. Thus, impurities can be removed from the plasma, which leads to better confinement. The experiment is usually run with deuterium as plasma fuel. Main characterizing parameters of the experiment are listed in table 1.1.

Although the particles are confined on the flux surfaces, they can break out of their orbits due to Coulomb collisions. This leads to a transport of heat and particles and thus to a reduction of the energy confinement time τ_E. In addition, the transport in toroidal plasmas is enhanced by the inhomogenity of the magnetic field, which is described by the so-called neoclassical transport. However, the experimentally measured transport in tokamaks is usually even higher than suggested by the neoclassical theory. This effect is attributed to the presence of plasma turbulence and the associated turbulent transport.

Parameter	Value
Total height of the device	9 m
Major plasma radius	1.65 m
Minor plasma radii	0.5 m
Magnetic field	3.2 T
Plasma current	1.2 MA
Pulse length	10 s
Plasma volume	13 m^3
Plasma temperature	100 $\cdot 10^6$ °C

Table 1.1: ASDEX Upgrade technical data.

Nowadays, computationally expensive numerical simulations aim to predict turbulence and turbulent transport in fusion plasmas. The most advanced description for the core plasma is the gyrokinetic theory. This approach exploits the fast gyromotion of charged particles around magnetic field lines, whose frequencies are typically fast compared to time scales of turbulence. Hence, averaging over the gyromotion can reduce the kinetic plasma description by one dimension, which makes the simulations computationally easier to perform.

Experimentally, Doppler reflectometry diagnostics can be used for turbulence investigation. In this method, an electromagnetic beam in the microwave frequency range is injected into the plasma. The beam is back-scattered by the turbulent fluctuations at the so-called cut-off layer similar to scattering at a diffraction grid. In contrast to conventional reflectometry, where the beam is injected perpendicular to the cut-off layer, Doppler reflectometry injects the beams at an oblique angle. This allows localized measurements of the perpendicular wavenumber spectrum $S(k_\perp)$, the perpendicular propagation velocity of density fluctuations $v_\perp$ and the radial correlation length l_r.

Since a diagnostic response can be very complex, often synthetic diagnostics are employed. For Doppler reflectometry full-wave codes are used, simulating the microwave beam propagation including the wave-plasma interaction. Additionally, synthetic diagnostics can lead to further understanding of non-trivial diagnostic effects due to wave propagation and the complex scattering processes in the experiment.

Non-trivial, non-linear effects concerning the perpendicular wavenumber spectrum were already investigated in experiment and simulation [6, 7]. Both consistently confirm different results as a function of beam polarization due to varying scattering conditions.

The perpendicular velocities have also been investigated in various fusion devices

by means of reflectometry. In the recent past, some of them could identify poloidal asymmetries [8, 9, 10], some could not [11]. In order to determine potential diagnostic effects, this thesis provides comprehensive studies of $v_\perp$ using a synthetic Doppler reflectometry diagnostic. The presented results investigate synthetic random phase turbulence. Preliminary results on AUG turbulence from gyrokinetic simulations are presented in the outlook.

Chapter 2 and 3 will provide the theoretical background regarding turbulence in plasmas and the Doppler reflectometry diagnostic, respectively. The simulation results are obtained using self generated synthetic turbulence in slab geometry and circular geometry. Therefore chapter 4 will provide information on the numerical generation of turbulence. Chapter 5 will present the analytical modeling of Doppler reflectometry, including the description of the used full-wave code IPF-FD3D. Finally, the results will be presented in chapter 6 followed by a summary and an outlook in chapter 7.

2 Turbulence

Turbulent flow can be described as chaotic or unsteady fluid movement. It is in opposite to laminar flows, which are characterized by flow sheets that move parallel to each other undisturbed. Turbulence is usually driven by gradients in e.g. pressure, density or temperature that lead to micro-instabilities. When these instabilities are amplified, non-linear processes cause a broad redistribution of energy and turbulence develops.

Incompressible neutral fluids, where $\nabla \cdot \mathbf{u} = 0$, can be described by the Navier-Stokes equation

$$\rho_m \left(\frac{\partial}{\partial t} + (\mathbf{u} \cdot \nabla) \right) \mathbf{u} = -\nabla p + \eta \Delta \mathbf{u}, \tag{2.1}$$

where $\mathbf{u}$ is the fluid velocity, ρ_m the mass density, p the pressure and η the viscosity. By normalizing the contributing quantities to the characteristic system sizes, the dimensionless Reynolds number Re can be deduced:

$$Re = \frac{\rho_m}{\eta} U_0 L. \tag{2.2}$$

Here, U_0 is the characteristic fluid velocity and L is the characteristic size of the system. It can be used to estimate the intensity of turbulence in a system, by expressing a ratio between non-linearity and viscosity. Figure 2.1 shows the transition from laminar to turbulent flow around an obstacle with increasing Reynolds number. Vortices are carried by the flow and form a so-called *Kármán vortex street*. As the Reynolds number increases further, the vortices start to interact with each other and end up in a fully developed turbulence. The turbulent vortices are characterized by their wavenumber k, the inverse of which is approximately equal to the vortex size $L \propto 1/k$.

This chapter first introduces the concept of the *turbulence wavenumber spectrum*, which is another important way of characterizing turbulence. Secondly, the effects of plasma currents on turbulence are discussed with the aim of motivating the measurement of plasma velocities.

2.1 Turbulence wavenumber spectrum

One of the main interests in the field of turbulence is the distribution of energy across different vortex scales, which are characterized by their wavenumber k. This distribution is called the *turbulence wavenumber spectrum*. Usually, energy is injected into the system by external or internal instabilities in a certain injection range k_{inj}. With time, the vortices merge or split due to non-linear interactions
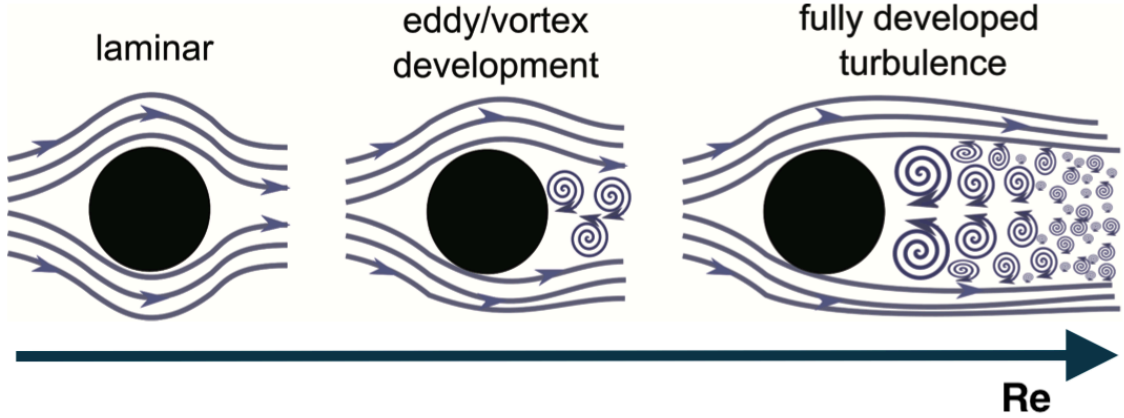
Figure 2.1: Sketch of fluid flow for different Reynolds numbers. With increasing Reynolds number turbulence develops from laminar flow through Kármán vortex streets. (adapted from [4])

between the different scales whereby energy is transferred. The modifications form cascades $\propto k^{-\alpha}$ in the wavenumber spectra, where α is called the spectral index. At some very small vortex sizes, energy is dissipated to the system, usually in the form of heat.

Turbulence structures are correlated in space and time. The spatial correlation is defined by the turbulence correlation length l, which is related to the average size of the turbulence structure. Temporal correlation is specified by the decorrelation time τ_d, giving an estimate for the mean life time of the fluctuations.

For homogeneous, isotropic three-dimensional (3D) turbulence, the turbulent wavenumber spectrum can be described by the so-called Kolmogorov spectrum [12], shown schematically in figure 2.2 (a). From dimensional analysis using energy conservation it can be derived that the distribution follows a direct cascade, where energy is transferred towards smaller scales:

$$E(k) = C\epsilon^{2/3}k^{-5/3} \quad \text{for } k > k_{inj}, \tag{2.3}$$

where C is a constant and ϵ the rate of energy dissipation.

In magnetic fusion plasmas mainly two-dimensional (2D) turbulence is observed. The electrons are exposed to rapid streaming along the magnetic field lines, so that the turbulence in the poloidal plane is more significant and $k_\perp \gg k_\parallel$. Here, as in the following, the subscripts parallel ($\parallel$) and perpendicular ($\perp$) refer to the background magnetic field. Vortex interactions in 3D turbulence, such as vortex stretching, do not occur in 2D. Thus, an additional conservation of vorticity Ω and thereby enstrophy $W \propto \Omega^2$ lead to the formation of new scaling laws [13].

For neutral fluids in 2D a Kolmogorov-Kraichnan wavenumber spectrum, as sketched in figure 2.2 (b), is observed. It is characterized by a *dual cascade*, obtaining two different spectral indices, regarding one inverse energy and one direct enstrophy
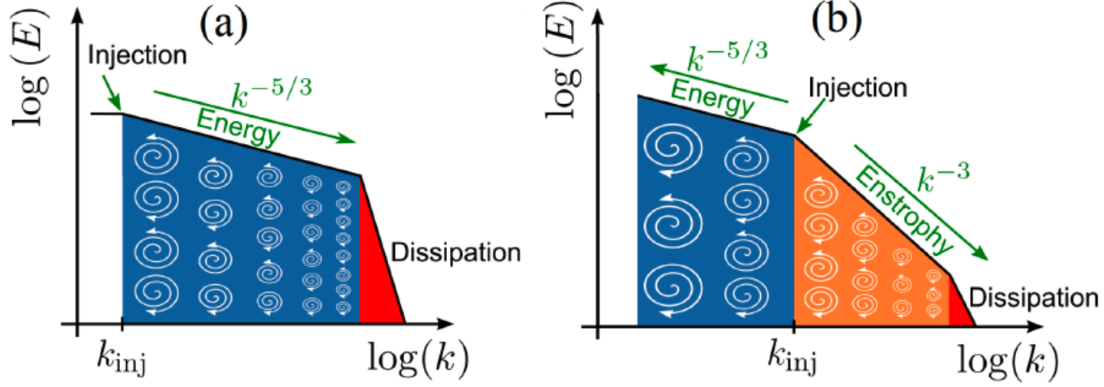
Figure 2.2: Turbulence wavenumber spectra of isotropic neutral fluids. (a) The Kolmogorov spectrum for 3D fluids with a direct energy cascade. (b) The Kolmogorov-Kraichnan spectrum for 2D fluids with a dual cascade for energy and enstrophy transfer. (adapted from [14])

cascade:

$$E(k) = \begin{cases} C\epsilon^{2/3}k^{-5/3} & \text{for } k < k_{inj}, \\ C\epsilon_\Omega^{2/3}k^{-3} & \text{for } k > k_{inj}, \end{cases} \tag{2.4}$$

where ϵ_Ω is the rate of vorticity dissipation. The k_{inj} is often referred to as the position of the *spectral knee*.

In fusion plasmas radial gradients in several parameters lead to a loss of isotropy. Therefore $k_\perp$ and k_r have to be used for turbulence characterization and the turbulence spectrum becomes a two-dimensional function. Perpendicular refers in this context to the direction perpendicular to the background magnetic field and to the flux surfaces. In the following, the power spectrum will by described by

$$E(k_r, k_\perp) \propto |h(k_r, k_\perp)|^2 (\delta n/n)^2, \tag{2.5}$$

where $|h(k_r, k_\perp)|^2$ is the 2D wavenumber spectrum and $(\delta n/n)$ is the turbulence fluctuation level. Doppler reflectometry, which is the main diagnostic investigated in this work, provides one dimensional wavenumber spectra regarding the perpendicular coordinate $E(k_\perp)$.

The presence of electron and ion motions, as well as the overlap of various instabilities driving the turbulence, increase the complexity as well. Nevertheless, the experimentally determined wavenumber spectra of fusion plasmas are generally Kolmogorov-like. They differ only in their spectral indices and knee positions, which can be useful to obtain information about the underlying instability.

2.2 Turbulence suppression by sheared flows

In 1982 *Wagner et al.* discovered a turbulent transport barrier at the tokamak experiment ASDEX [15]. The new operation mode was called *high confinement*

mode (H-mode) and is characterized by said barrier, which reduces particle and heat transport. This leads to an increase in confinement time of a factor 2 to 3. In contrast to the standard *low confinement mode* (L-mode), the barrier comes with much steeper gradients of density and temperature at the plasma edge.

The transition from L-mode to H-mode is nowadays believed to be triggered by a gradient in the radial electric field E_r [16], which leads to sheared plasma flows due to the $E \times B$ drift

$$v_{E \times B} = \frac{E \times B}{B^2}.$$ (2.6)

Since the drift is independent of the charge, it generates bulk plasma movement, which also carries the turbulent structures. Thus, they move in perpendicular direction with a velocity of

$$v_\perp = v_{E \times B} + v_{ph},$$ (2.7)

where v_{ph} is the additional phase velocity of the density fluctuations in the plasma frame, that is dependent on the turbulent structure size.

It is commonly assumed that turbulence vortices, when subjected to strong shear flows, are first tilted and stretched and then torn apart, reducing the radial correlation length and thus the turbulent diffusion step size. This leads to a decrease in turbulence amplitude and transport [16]. The decorrelation mechanism is illustrated in figure 2.3. However, energy is only redistributed onto smaller scales, rather than extracted from the turbulence.

Energy transfer can occur through the general tilting and stretching of vortices due to negative viscosity, the so-called Reynolds stress [17]. This mechanism drives zonal flows, which are low-frequency poloidal and toroidal symmetric electrostatic fluctuations, and thus do not involve radial transport. Nevertheless, since zonal flows can be driven by turbulence, a reduction in the turbulence level will also lead to a reduction in energy transfer into zonal flows. Accordingly, comprehensive modeling is needed to fully capture this complex interplay.

The formation of such transport barriers like for the L-H-transition through the E_r gradient are still under investigation. Thus, experimental and numerical investigations regarding the turbulent structures and their perpendicular velocities $v_\perp$ are of great interest.
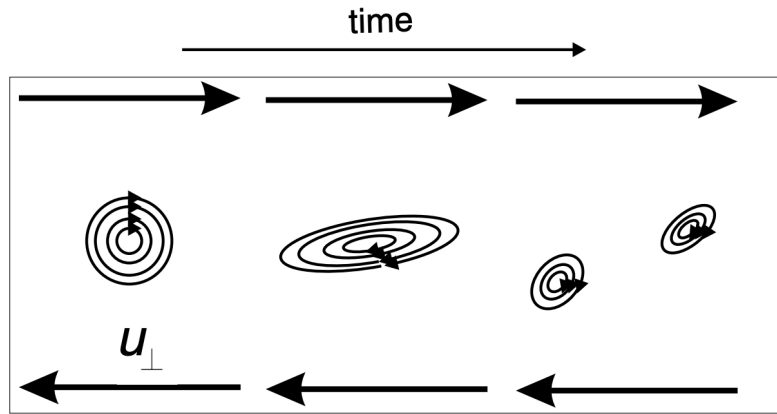
Figure 2.3: Decorrelation mechanism due to sheared flows. The vortex is stretched, tilted and finally split up. (adapted from [18])

3 Doppler reflectometry

Microwave reflectometry is a common diagnostic technique used to analyze the electron density and its turbulent fluctuations in fusion plasmas. In conventional reflectometry electromagnetic beams are radiated perpendicular to the so-called cut-off layer, where they are reflected from the plasma. By successively increasing the frequency, the wave penetrates deeper into the plasma and a scan of the density is obtained. In contrast, Doppler reflectometry exploits the back-scattering of electromagnetic waves at density fluctuations by using obliquely incident beams. Thus, the diagnostic provides spatially, temporally and wavenumber-resolved information about the power of density fluctuations and, exploiting the effect of the Doppler shift, also the measurement of their velocity.

First, this chapter gives an introduction on relevant theory of wave propagation in plasmas. This is followed by a section focusing on the physical mechanism of Doppler reflectometry. Relevant discussions on spectral and spacial resolution of the measurements are given, followed by a description of the ASDEX Upgrade Doppler reflectometer.

3.1 Electromagnetic wave propagation in plasmas

Waves are usually considered as periodic disorders of equilibrium parameters

$$\psi(\mathbf{r}, t) = \psi_0(\mathbf{r}) + \psi_1 \exp(i\mathbf{k} \cdot \mathbf{r} - i\omega t), \tag{3.1}$$

with the wave vector $\mathbf{k}$, denoting the direction of propagation of the wave and its frequency ω.

The behavior of electromagnetic waves is determined by Maxwell's equations that can be used to derive the wave equation:

$$\nabla \times (\nabla \times \mathbf{E}) = -\frac{\omega^2}{c^2} \hat{\boldsymbol{\epsilon}}(\omega)\mathbf{E}, \tag{3.2}$$

where $\mathbf{E}$ is the wave's electric field, $\hat{\boldsymbol{\epsilon}}(\omega)$ is the complex dielectric tensor and c is the speed of light. In order to determine the dielectric tensor for Doppler reflectometry, some prior assumptions are usually made.

Reflectometry diagnostics in plasma physics typically deal with frequencies in the microwave range (GHz). Hence, the thermal velocity of the electrons is far below the wave's velocity $v_{th} \ll \omega/k$, so for the wave description the so-called *cold plasma approximation* is used, where pressure contributions are neglected. Furthermore, the applied frequencies are much higher than the ion plasma ω_{pi} and cyclotron ω_{ci} frequencies, so that the plasma response is defined by the electrons only.

3. Doppler reflectometry

Considering these assumptions, the dielectric tensor in cold plasma approximation equals:

$$\hat{\epsilon}(\omega) = \begin{pmatrix} S & -iD & 0 \\ iD & S & 0 \\ 0 & 0 & P \end{pmatrix}, \qquad \begin{aligned} S &= 1 - \frac{\omega_{pe}^2}{\omega^2 - \omega_{ce}^2}, \\ D &= -\frac{\omega_{ce}}{\omega} \frac{\omega_{pe}^2}{\omega^2 - \omega_{ce}^2}, \\ P &= 1 - \frac{\omega_{pe}^2}{\omega^2}. \end{aligned} \qquad (3.3)$$

Therefore, the wave propagation depends on the local background electron density n_e and the magnetic field B_0 through the electron plasma ω_{pe} and cyclotron ω_{ce} frequencies:

$$\omega_{pe} = \sqrt{\frac{n_e e^2}{\epsilon_0 m_e}}, \qquad\qquad \omega_{ce} = \frac{e B_0}{m_e}. \qquad (3.4)$$

For geometrical reasons, the wave in the experiment is launched perpendicular to the background magnetic field. Consequently, for Doppler reflectometry only those modes are of interest where $\mathbf{B} \perp \mathbf{k}$.

Assuming a coordinate system with $\mathbf{B_0} = B_0 \hat{\mathbf{e}}_z$ and using the wave approach (3.1) for the electric field, after some rearrangements the wave equation (3.2) becomes:

$$\begin{pmatrix} N^2 - S & -iD & 0 \\ iD & -S & 0 \\ 0 & 0 & N^2 - P \end{pmatrix} \begin{pmatrix} E_{1x} \\ E_{1y} \\ E_{1z} \end{pmatrix} = 0. \qquad (3.5)$$

Here, the refractive index $N = |\mathbf{N}| = |c\mathbf{k}/\omega|$ is introduced. If the refractive index approaches zero ($N = 0$), the wave vector will change its sign and the wave is reflected.

There are two non-trivial solutions for the determinant of the matrix (3.5) to be zero, that correspond to the two different propagation modes. The *ordinary mode* (O-mode), where the wave's electric field is parallel to the background magnetic field ($\mathbf{E_1} \parallel \mathbf{B_0}$) and the *extraordinary mode* (X-mode), where the wave's electric field is perpendicular to the background magnetic field ($\mathbf{E_1} \perp \mathbf{B_0}$).

Hence, for the O-mode, the refractive index describing the wave propagation results from the last line of (3.5):

$$N_{\mathrm{O}}^2 = \left(1 - \frac{\omega_{pe}^2}{\omega^2} \right). \qquad (3.6)$$

The cut-off frequency, which is the frequency where N_{O} approaches zero, is equal to the plasma frequency $\omega_{\mathrm{O,co}} = \omega_{pe}$. Thus, it only depends on the electron density

n_e. The cut-off layer, where the wave is reflected, will be therefore parallel to the magnetic flux surfaces ρ_{pol} in the plasma.

For the X-mode the refractive index follows from the upper two equations and is given by

$$N_{\mathrm{X}}^2 = 1 - \frac{\omega_{pe}^2}{\omega^2} \cdot \frac{\omega^2 - \omega_{pe}^2}{\omega^2 - \omega_{ce}^2 - \omega_{pe}^2}. \tag{3.7}$$

Remark here, that an additional dependency on the magnetic field is present due to the electron cyclotron frequency. Hence, the cut-off layers are not necessarily aligned with the magnetic flux surfaces.

3.2 Physical mechanism of Doppler reflectometry

The mechanism of Doppler reflectometry, also called Doppler back-scattering, is illustrated in the figure 3.1. It shows the cross-section of the plasma on the left and the launching and receiving antenna on the right. It is located outside of the plasma in vacuum, where the refractive index is $N = 1$. The incident beam enters the plasma with an oblique angle θ with respect to the cut-off surface normal. As the beam approaches denser plasma, the refractive index decreases according to the dispersion relation and is thus bent until it is reflected at the cut-off layer. At this point, the refractive index is minimal and the beam is completely parallel to the cut-off surface.

If turbulent density fluctuations are present, a part of the wave is also back-scattered at the turbulent structures, similar to back-scattering at a diffraction grid. Due to the amplification of the microwave field at this turning point, the signal relates predominantly to this region.

The main signal corresponds to fluctuations from $\mathbf{k_{fl}}$, which fulfill the $m = -1$ Bragg condition

$$\mathbf{k_{fl}} = -2\mathbf{k_i} = -2\mathbf{N}k_0, \tag{3.8}$$

where $\mathbf{N}$ is the refractive index, $\mathbf{k_i}$ the wavenumber of the incident beam at the tuning point and k_0 the vacuum wavenumber $k_0 = 2\pi f_0/c$. However, due to the extended beam size there are also contributions of other $\mathbf{k}$ close to $\mathbf{k_{fl}}$ in the scattering region. Consequently, the spectral Δk and spatial Δr resolutions of the probe are of special interest.

For slab geometry, i.e. flat refractive index layers, the refractive index at the turning point is simply $N = \sin\theta$. For curved geometries, as in the experiment, ray-tracing techniques have to be used in order to evaluate $N^2 = N_\perp^2 + N_\parallel^2$ to determine the minimum N.

The power of the back-scattered wave P depends on the turbulence amplitude $(\delta n/n_0)$, where n_0 is the background density. For sufficiently low turbulence levels, usually below 1% of the background density, the response is said to be *linear*, corresponding to single scattering events.

$$P \propto (\delta n/n_0)^2 h(k)^2, \tag{3.9}$$
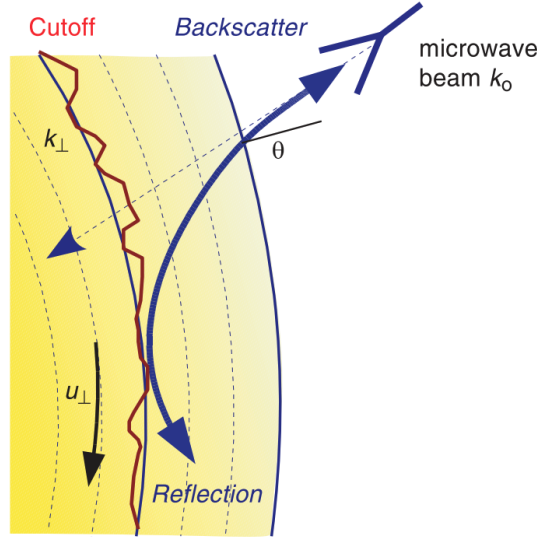
Figure 3.1: Sketch of the Doppler reflectometer's microwave beam path. The beam enters the plasma from an antenna with oblique angle θ. In addition to the beam's reflection, a part of the wave is back-scattered at the turbulence structures at the cut-off. (adapted from [20])

where $h(k)$ is the underlying turbulence spectrum. However, real fusion plasmas can have significantly higher turbulence levels of 5-10 % and thus enter into a *non-linear* response regime. In this case, significantly more power is back-scattered by multiple scattering events.

Since the density fluctuations in fusion plasmas are usually moving relative to the probing beam with a velocity $\mathbf{v}$, the back-scattered spectrum becomes Doppler shifted. The Doppler shift frequency is

$$\omega_D = \mathbf{v} \cdot \mathbf{k_{fl}} = v_\perp k_\perp + v_\parallel k_\parallel + v_r k_r \approx v_\perp k_\perp. \tag{3.10}$$

This approximation can be assumed because the radial and parallel terms are usually very small compared to the perpendicular term, since $k_\parallel \ll k_\perp$ and $k_r \to 0$ at the beam turning point.

As already stated in chapter 2, the actual measured perpendicular velocity $v_\perp = 2\pi f_D/k_\perp$ is:

$$v_\perp = v_{E \times B} + v_{ph}. \tag{3.11}$$

The magnitude and direction of the phase velocity can provide information about the underlying turbulence [19]. However, experiments and simulations have shown that v_{ph} is usually small compared to the $E \times B$ drift velocity. Assuming $v_{ph} \ll v_{E \times B}$ the radial electric field E_r can be determined from the perpendicular velocity. From (2.6) follows

$$E_r = v_\perp B. \tag{3.12}$$
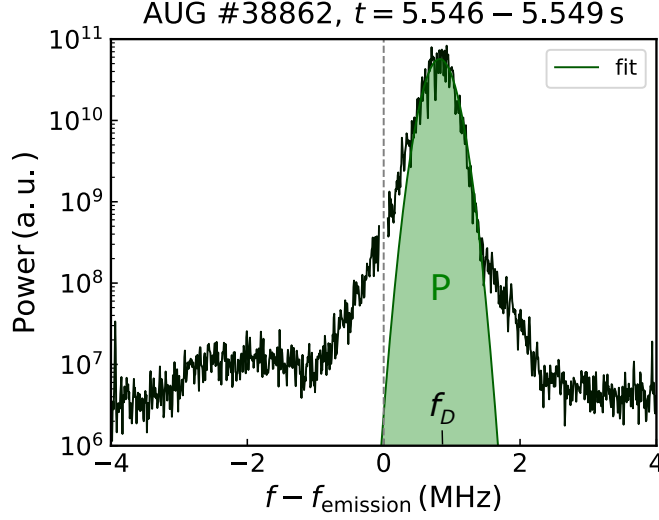
Figure 3.2: Doppler Spectrum from ASDEX Upgrade Doppler reflectometer (X-mode), including a Gaussian fit. The integral of the fit is the back-scattered power P. The Doppler shift f_D is used to determine the perpendicular velocity $v_\perp$.

A typical Doppler spectrum, obtained from a Doppler reflectometer is shown in figure 3.2. The spectrum is plotted in logarithmic scale on the y-axis. The peaks of the Doppler spectrum are fitted with a Gaussian function:

$$S(A, f_D, \sigma, f) = A \cdot e^{-\frac{(f-f_D)^2}{2\sigma^2}}. \tag{3.13}$$

Here, A is the peak amplitude, f_D the peak position and therefore the Doppler shift frequency. σ is the peak width with approximately 68% of the complete peak's area.

The turbulence powers are determined by integrating the fitted Gaussian. This power is measured for multiple wavenumbers at the same radius. Plotting the back-scattered power P against the probed wavenumber $k_\perp$ gives the turbulence power spectrum. The Doppler shift frequency f_D is needed to determine the perpendicular velocities $v_\perp$ and can be obtained directly from the fit parameters. Thereafter, the perpendicular velocity can be obtained by (3.10).

3.3 Spectral and spatial resolution

The launched microwave beam can be approximated to be Gaussian, characterized by a beam waist w_0 at the beam's focus. For an input vacuum wavenumber k_0, the spectral resolution is given by [21]

$$\Delta k(w_{0,\text{eff}}, R_c, R_b, k_0) = \frac{2\sqrt{2}}{w_{0,\text{eff}}} \sqrt{1 + \left(\frac{w_{0,\text{eff}}^2 k_0}{\rho_{\text{eff}}}\right)^2}. \tag{3.14}$$

Here, $w_{0,\text{eff}}$ denotes the effective beam waist $w_{0,\text{eff}} = w_0/\cos(\theta)$. This includes the effect of geometric projection of the beam waist towards the reflecting layer, that is
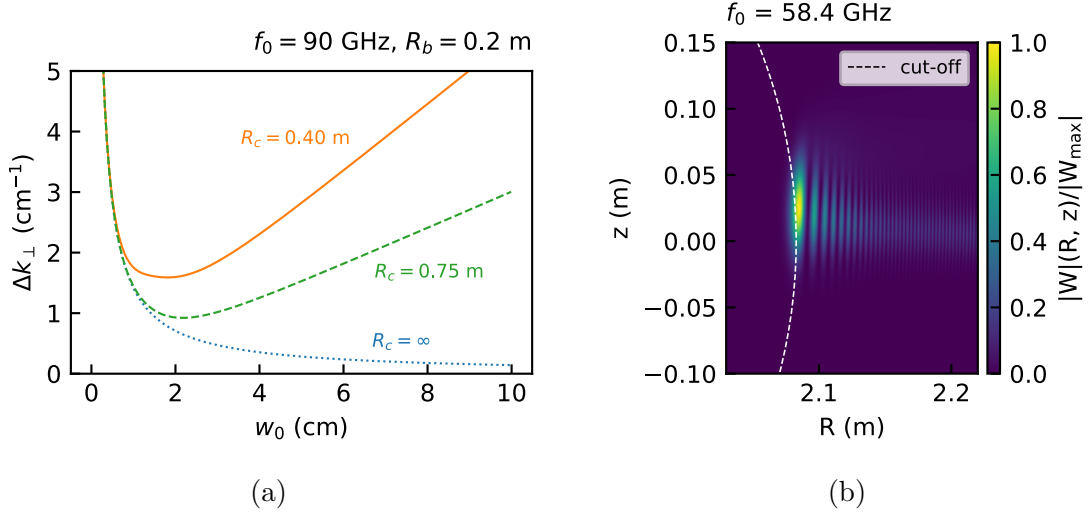
Figure 3.3: (a) Dependence of the spectral resolution on the beam waist w_0 for different plasma curvature radii. For finite curvature radii an optimal beam waist exists. (b) Weighting function, that is computed using full-wave simulations for a beam of $f_0 = 58.4\,\text{GHz}$. The antenna is located at $(R, z) = (2.3, 0.0)\,\text{m}$ and is pointing slightly upwards.

caused by the oblique incidence with the angle θ. The effective radius ρ_{eff} is [22]

$$\rho_{\text{eff}} = \frac{2R_c R_b}{R_c + 2R_b}, \tag{3.15}$$

where R_c is the curvature radius of the plasma and R_b is the beam curvature radius at the cut-off layer. The latter can be derived using the Gaussian beam equations:

$$R_b(z) = z(1 + (\frac{z_R}{z})^2). \tag{3.16}$$

Here, z is the covered track of the beam, which can be identified by using the raytracing techniques and $z_R = w_{0,\text{eff}}^2 / 2k_0$.

For slab geometry $R_c = \infty$. Therefore, (3.14) reduces to

$$\Delta k = \frac{2\sqrt{2}}{w_{0,\text{eff}}}. \tag{3.17}$$

For wider beams the spectral resolution gets finer. This is shown by the blue dotted line in figure 3.3(a).

For circular and ASDEX Upgrade geometry, plasma and beam curvature radii have to be taken into account. Thus, an optimal beam waist exists, for which the spectral width Δk is minimal. Setting the first derivative of (3.14) to zero leads to

$$w_{\text{opt}} = \sqrt{\frac{\rho_{\text{eff}}}{k_0}}. \tag{3.18}$$

Since the optimal beam waist depends on the input wavenumber, the incident angle and the propagation distance the used beam waist can not be perfect for all frequencies. Figure 3.3(a) shows the spectral resolution for two different finite curvature radii, that correspond to the circular geometry used in the following ($R_c = 0.40\,\mathrm{m}$) and the AUG geometry ($R_c = 0.75\,\mathrm{m}$). The curves clearly show, that larger curvature radii can significantly improve the spectral resolution.

Alternatively, the spectral and spatial resolutions can be determined by analyzing the so-called *weighting function* using full-wave simulations [23]. For a mono-static antenna configuration, as used for Doppler reflectometry, the complex weighting function is:

$$W(\mathbf{r}) = < E^2(\mathbf{r}, t) >, \tag{3.19}$$

where E is the complex incident probing electric field. $< \cdot >$ denotes the time averaging over a microwave period. The weighting function determines for each point in space the phase and amplitude with which an elementary emitter (δn) would contribute to the main signal. A typical 2D weighting function for a beam with $f_0 = 58.4\,\mathrm{GHz}$ approaching the plasma from the right is shown in figure 3.3(b) for a plasma in circular geometry. The spatial resolution can be determined directly from the spatial extent of the weighting function due to the Gaussian fit around the inflection point of the beam. The contour shows that the maximum of the weighting function, corresponding to the dominant back-scattered signal, is slightly shifted towards the plasma edge, compared to calculations done by raytracing. This also leads to a slightly different probed k_0, than predicted by raytracing. The actual wavenumber and its spectral resolution Δk can be determined by Fourier analysis of the weighting function at the maximum position.

3.4 Heterodyne detection

Doppler reflectometry usually uses heterodyne detection [24] to obtain the back-scattered field. Thus, the received signal S has two components, an in-phase I and a quadrature Q part:

$$I(t) = A(t)\cos(\phi(t)), \tag{3.20}$$
$$Q(t) = A(t)\sin(\phi(t)). \tag{3.21}$$

The combined complex signal, that is used for further analysis is

$$S(t) = I(t) + iQ(t) = A(t)e^{i\phi(t)}. \tag{3.22}$$

Thus, the amplitude A and phase ϕ can be determined separately:

$$A(t) = \sqrt{I(t)^2 + Q(t)^2}, \tag{3.23}$$
$$\phi(t) = \pm\arctan\left(\frac{Q(t)}{I(t)}\right). \tag{3.24}$$

4 Turbulence modeling

In the following, Doppler reflectometry is investigated theoretically using simulations. These *synthetic* experiments require artificial turbulence.

All of the simulations shown in this thesis are based on isotropic and anisotropic synthetic turbulence. In this way, simple geometries can be studied where a constant bulk velocity is modeled by continuously shifting the entire static turbulence pattern. The comparison between the input parameters and the results is straightforward. However, since the synthetic turbulence omits a lot of the complexity of realistic fusion plasmas, further investigations need gyro-kinetic turbulence simulations based on experimental data. Thus, it allows direct comparison to the experiment. The turbulence includes self-generated radially sheared plasma flows, including an intrinsic phase velocity of the turbulence structures and realistic intermittent time behavior.

This section focuses first on the generation of synthetic turbulence and its velocity for simple geometries. Turbulence spectra used in further analysis are presented, followed by an introduction to gyro-kinetic turbulence.

4.1 Synthetic turbulence

4.1.1 Turbulence generation

The turbulence is created from initially set two-dimensional wavenumber spectra $h(k_R, k_z)$, where k_R and k_z are the wave vectors in both dimensions of the (R, z) poloidal plane. For Kolmogorov-like *realistic spectra* this has the form

$$h(k_R, k_z) = \begin{cases} k^{-\eta_1} & \text{if } |k| \leq k_{\text{knee}}, \\ k^{-\eta_2} & \text{else}, \end{cases} \tag{4.1}$$

where $|k| = \sqrt{k_R^2 + k_z^2}$. The spectrum is shown in figure 4.1 for $k_R = 0$. Note that following equation (3.9) a spectral index η in the turbulent wavenumber spectrum will correspond to a spectral index of $\alpha = \eta^2$ in the final power spectrum P.

To avoid coherent signals, random complex phases are added on the spectra, so that

$$h(k_R, k_z) = |h(k_R, k_z)|\, e^{i\phi(k_R, k_z)}, \quad \phi \in [0, 2\pi] \text{ uniformly random}. \tag{4.2}$$

In contrast to realistic turbulence, that is anisotropic and shows intermittent time behavior, the generated synthetic turbulence is isotropic and static.

By applying an inverse two-dimensional Fourier transform to the spectrum the turbulence field is generated.

$$\delta n(R, z) = \iint \mathrm{d}k_R\, \mathrm{d}k_z h(k_R, k_z)\, e^{ik_R R + ik_z z}. \tag{4.3}$$

4. Turbulence modeling
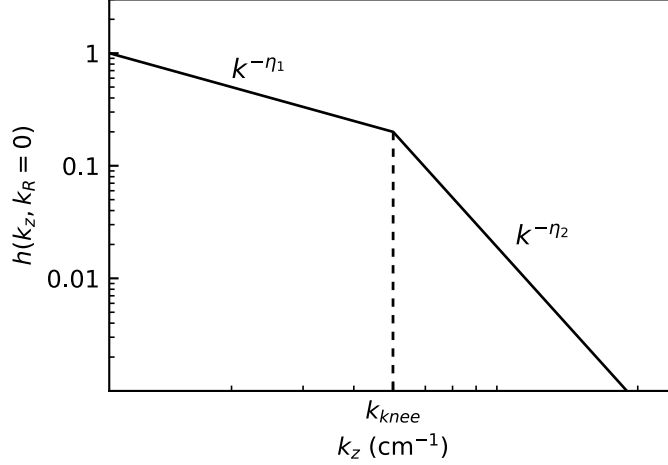
Figure 4.1: Kolmogorov-like turbulence spectrum in 1D as described in (4.1).

Afterwards the turbulence is normalized to the background density.

$$\delta n(R, z)_{\text{final}} = \frac{\delta n(R, z)}{\sigma_{\delta n}} n_0(\rho_{\text{probe}}), \tag{4.4}$$

where $\sigma_{\delta n}$ is the standard deviation of $\delta n(R, z)$ and ρ_{probe} the magnetic flux surface where the turbulence structures are investigated.

A 2D wavenumber spectrum for $\eta_1 = 0$, $\eta_2 = 2$ and $k_{\text{knee}} = 5\,\text{cm}^{-1}$ is shown in figure 4.2(a). A segment of the resulting turbulence pattern is shown in figure 4.2(b).

In addition to the Kolmogorov-like spectrum, a Gaussian turbulence spectrum is used for the full-wave simulations, which allows for anisotropic structures. The Gaussian wavenumber spectrum is taken from [25] and is given by

$$|h(k_R, k_z)| = \frac{l_{\min} l_{\max}}{8\pi} \exp\left[-\frac{(k_R \cos\beta - k_z \sin\beta)^2 l_{\max}^2 + (k_R \sin\beta + k_z \cos\beta)^2 l_{\min}^2}{8}\right], \tag{4.5}$$

where β is the tilt angle with respect to the R-axis. $l_{\min}$ and $l_{\max}$ are the correlation lengths in R and z direction for $\beta = 0°$. All parameters are shown in figure 4.3(a). A turbulence pattern obtained using the presented spectrum is shown in figure 4.3(b) for a tilt angle of $\beta = 30°$.

To properly recover the turbulence characteristics using the synthetic diagnostic, the turbulence is applied only as a turbulence band to the poloidal flux surface ρ_{pol} of interest. This is illustrated in figure 4.4. It is additionally masked with a Tukey window function.

20

<div align="center">(a)   (b)</div>
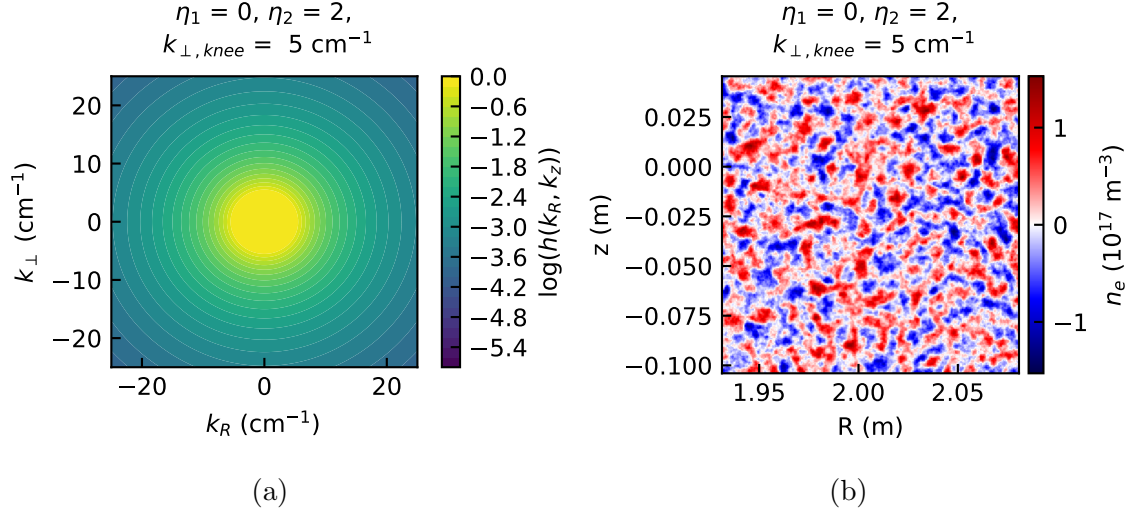
Figure 4.2: Generated synthetic turbulence for a realistic spectrum cf. (4.1) with $\eta_1 = 0$, $\eta_2 = 2$ and $k_{\text{knee}} = 5\,\text{cm}^{-1}$. (a) The 2D turbulence spectrum and (b) a segment of the turbulence pattern which is obtained by IFFT of (a).

<div align="center">(a)   (b)</div>
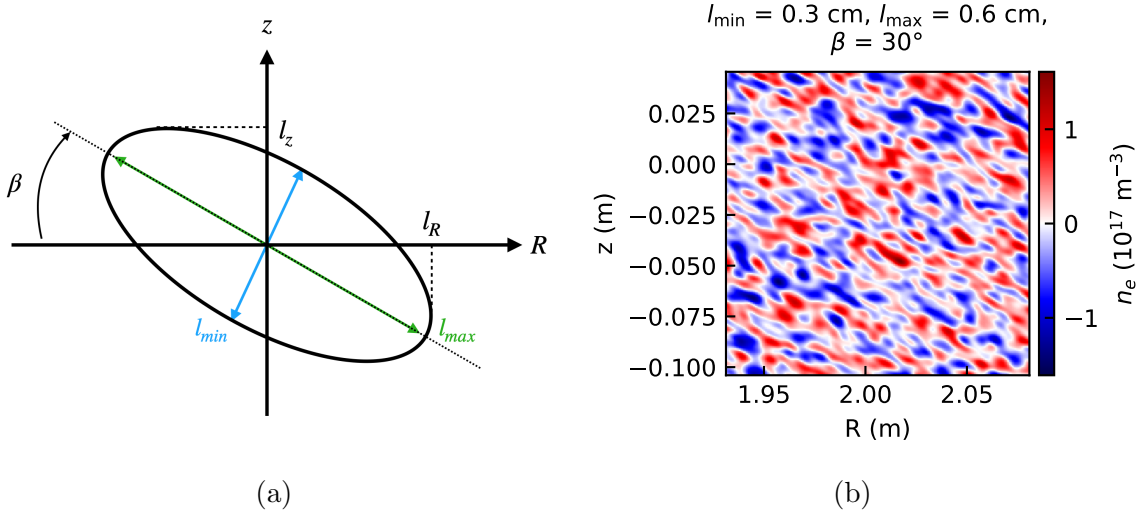
Figure 4.3: (a) Sketch of tilted turbulence structure, that can be generated using a Gaussian turbulence spectrum (4.5). (b) Anisotropic turbulence pattern, that is generated form (4.5) with $l_{\text{min}} = 0.3\,\text{cm}$, $l_{\text{max}} = 0.6\,\text{cm}$ and $\beta = 30°$.
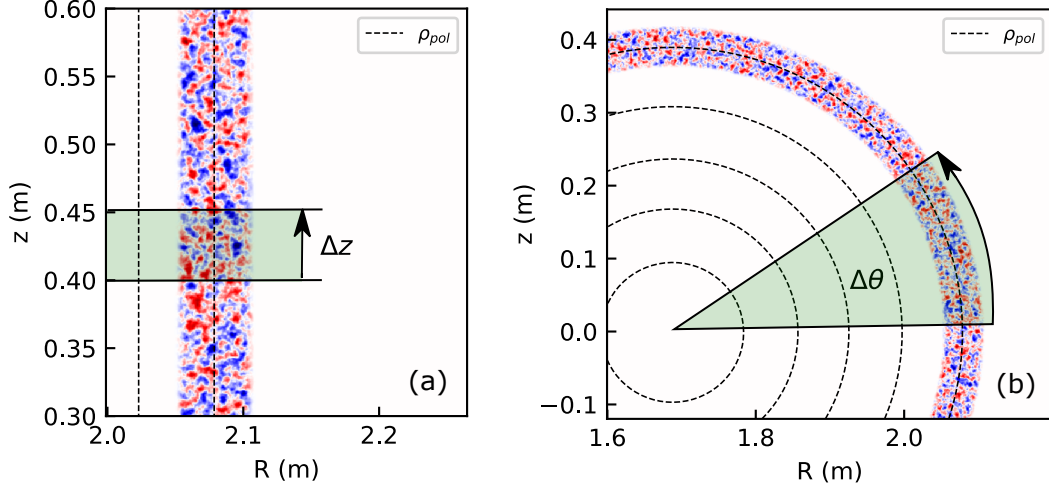
Figure 4.4: Schematic illustration of the velocity modeling for synthetic turbulence. The turbulence pattern is shifted or rotated by a constant Δz (slab) or $\Delta \theta$ (circular). In the scope of this thesis, the spatial shift is set to $1\,\mathrm{mm}$.

4.1.2 Perpendicular velocity modeling

The geometries used in the scope of this thesis are slab geometry and circular geometry, which are discussed in detail in chapter 6. For both geometries the density fluctuations movement is obtained by constantly shifting (slab) or rotating (circular) the turbulence pattern with a preliminary defined Δz or $\Delta \theta$, respectively.

This is schematically shown in figure 4.4(a) for slab geometry, where the implementation is straight forward.

For circular geometry, the turbulence pattern is rotated with respect to the plasma center, as shown in 4.4(b). The synthetic turbulence pattern obtained with (4.3) is rectangular. The desired turbulence band is cut out from a turbulence pattern that overlaps the entire geometry. Therefore, for a circular geometry, the synthetic diagnosis can only be applied to isotropic turbulence. Anisotropic structures will therefore rotate accordingly and further change the turbulence spectrum at the measurement point with each displacement. This can significantly complicate the analysis of the turbulence spectrum.

4.1.3 Turbulence correlation

The spatial correlation for the synthetic turbulence can be determined numerically. Therefore the cross-correlation is used on the turbulence pattern, comparing turbulence at R and $R + \Delta R$:

$$C(\Delta R; R, \Delta z) = \int \mathrm{d}z \delta n^*(R, z) \delta n(R + \Delta R, z + \Delta z), \qquad (4.6)$$

where * stands for the complex conjugate. The maxima of (4.6) $C_{\max}$ with respect to the displacement ΔR are plotted against each other. Determining the $1/e$ width

of $C_{\max}(\Delta R)$ by Gaussian fitting gives the correlation length l_R. Similarly, the same computation can be performed for the correlation in z-direction.

In case of the Gaussian turbulence spectrum (4.5) the correlation length is already defined directly in the initialization.

The correlation length of the turbulence is of interest because it plays a decisive role in determining the validity of linear scattering, which will be discussed in the section 5.1.
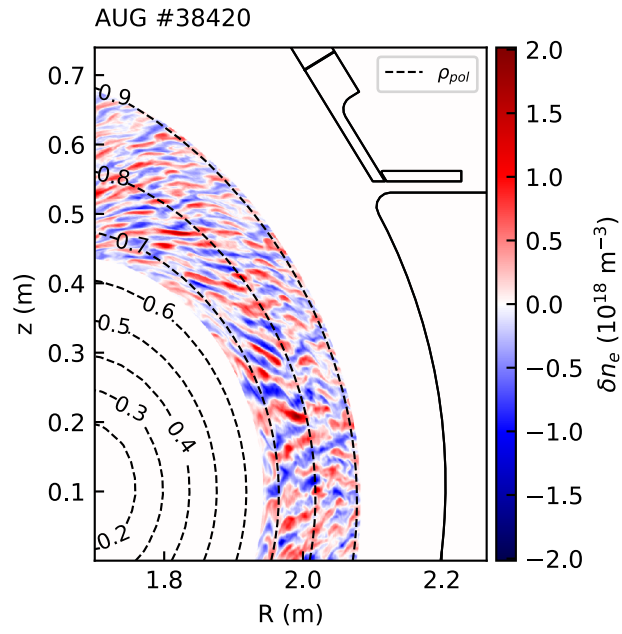
4.2 Gyrokinetic turbulence simulations

The modeling and prediction of turbulence for fusion plasmas in real geometries is very complex. Nowadays, the most appropriate theory to describe core plasma micro-turbulence in magnetized plasmas is the *gyrokinetic theory*. This approach exploits the gyro-motion of charged particles around magnetic field lines, reducing the 6D kinetic Vlasov equation by one dimension. This leads to a considerable reduction of the system's complexity.

The code, which produced the most realistic turbulence used in the scope of this thesis, is the gyrokinetic turbulence code GENE [26]. It can afford local (flux-tube) and global (full-torus) simulations of turbulence. Here, local simulations were used, as the global ones can be computationally demanding.

A segment of turbulence obtained by GENE for ASDEX Upgrade shot #38420 is shown in figure 4.5. It shows the more complex anisotropic, sheared structures in the D-shape geometry of AUG.

Figure 4.5: Turbulence pattern obtained by the gyro-kinetic turbulence simulation code GENE for AUG shot # 38420. The shown segment corresponds to the upper right part of the poloidal cross-section of AUG. The poloidal flux surfaces ρ_{pol} are shown in dashed black.

5 Doppler reflectometry modeling

To assess the Doppler reflectometry diagnostic power response and velocity measurements, theoretical modeling is inevitable. Reliable descriptions can already be obtained by analytical modeling under certain approximations. However, these neglect various wave effects (wave trapping, non-linear plasma-wave interaction, etc.) that may be important for realistic fusion plasmas, especially at high turbulence levels ($> 5\%$). Therefore, more complex time-dependent two-dimensional full-wave simulations are useful. They include all parts of the electromagnetic waves by solving Maxwell's equations directly in time and can thus capture wave effects even in strongly fluctuating plasmas.

This chapter will first introduce into linear and non-linear scattering theory and their validity limits. Then, the 2D full-wave simulation code IPF-FD3D, that was used in this thesis, is presented. The last section discusses analytically the influence of the turbulence wavenumber spectra on the velocity measurement.

5.1 Linear and non-linear power response

The dispersion relations discussed in section 3.1 only apply locally because the plasma parameters were assumed to be constant. Since real plasmas are not homogeneous, in the wave equation (3.2) a spatial dependence of the refractive index has to be taken into account. Assuming quasi-neutrality, i.e. $\nabla \cdot E = 0$, it turns out to be a Helmholtz-type equation. For O-mode polarization and in one dimension it has the form

$$\left[\frac{\partial^2}{\partial x^2} + k^2(x) \right] E = 0,$$ (5.1)

with $k(x) = N(x) \cdot \omega/c$.

The presence of density fluctuations further complicates the spatial dependence of the refractive index. However, if the fluctuation level is low enough so that $\epsilon = \delta n / n_0 \ll 1$, perturbation theory can be applied. The background density n_0 and the density fluctuations δn can be considered separately:

$$n = n_0 + \delta n.$$ (5.2)

Then, the full solution for E can be written as a power series $E = E_0 + E_1 \epsilon^1 + O(\epsilon^2)$, where E_0 is the unperturbed electric field. Applying (5.2) to (5.1) the first order terms are:

$$\left[\nabla^2 + k^2(x) \right] E_1 = -\frac{\omega^2}{c^2} \epsilon E_0.$$ (5.3)

5. Doppler reflectometry modeling

The linear approach assumes that $O(\epsilon^2)$ is negligible and is also known as the Born approximation [27]. The perturbed field E_1 corresponds the signal due to a single scattering event at the density fluctuations of interest only. By further analyzing higher orders of the perturbation (ϵ^2, ϵ^3, etc.), the total back-scattered field E can be successively derived.

In the Born approximation, the complete back-scattered signal corresponding to the Doppler reflectometer output can be derived employing the reciprocity theorem [28],

$$I(t) + iQ(t) = C \int \mathrm{d}\mathbf{r} E_0^2(\mathbf{r}) \frac{\delta n(\mathbf{r}, t)}{n_c}, \tag{5.4}$$

where C is a dimensionless constant and n_c the background density at the wave's cut-off. The integral in (5.4) requires knowledge on the unperturbed electric field E_0. When E_0 is known, the signal can be computed for each turbulence realization for further processing using the same analysis routines as for experimental data.

E_0 can be obtained solving the unperturbed Helmholtz equation (5.1). For simple density profiles, solutions can be found analytically by using the Green's function [29]. However, realistic plasma background parameters usually require numerical methods.

In fusion plasmas, linear scattering is mostly observed when probing in the core region, where the turbulence level is low $\epsilon < 0.1\%$. However, the transition from linear to non-linear scattering does not only depend on the turbulence level, such that theoretical estimates are useful. For normal incidence reflectometry the linear theory was found to be valid for [30]
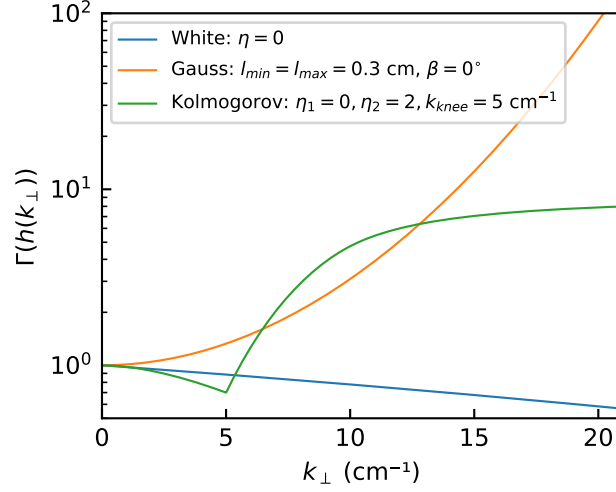
$$\gamma = \left(\frac{\delta n}{n_0}\right)^2 \frac{G^2 \omega_0^2 L^{\mathrm{ref}} l_R}{c^2} \ln\left(\frac{L^{\mathrm{ref}}}{l_R}\right) \ll 1. \tag{5.5}$$

Here, $L^{\mathrm{ref}} = (\nabla N_0/N)$ is the refractive index gradient scale length, $\omega_0 = 2\pi f_0$, l_R and c are the probing frequency, the radial correlation length and the speed of light in vacuum, respectively. The enhancement factor G taking into account the wave's polarizations is

$$G = \begin{cases} 1 & \text{for O-mode,} \\ \dfrac{\left(\omega_0^2 - 2\omega_{pe}^2\right)\left(\omega_0^2 - \omega_{ce}^2\right) + \omega_{pe}^4}{\left(\omega_0^2 - \omega_{pe}^2 - \omega_{ce}^2\right)^2} & \text{for X-mode.} \end{cases} \tag{5.6}$$

Accounting the so-called physical optics (PO) model [31], a similar critical turbulence level σ_c can be derived. The model assumes slab geometry with a corrugated reflection layer which represents the turbulence. It provides an alternative expression for the the complete back-scattered signal, including a dependency on the inflection angle θ. However, other than perpendicular incidence in equation (5.4), the PO model does not account for the density and magnetic field gradient of the plasma.

Joining both, the critical turbulence level of the PO model and the Born approximation approach, forms a new criteria. This combines the dependency on the

Figure 5.1: Convolution term (5.8) for three different turbulence spectra. Γ reduces the non-linearity factor γ cf. (5.7) for the white spectrum. For Kolmogorov-like and Gaussian spectra, which exhibit a spectral decay, γ increases strongly, especially for high wavenumbers. This reduces the critical turbulence level that marks the transition to the non-linear regime.

background electron density and magnetic field with oblique incidence probing [32]:

$$\gamma = \left(\frac{\delta n}{n_0}\right)^2 \frac{G^2 \omega_0^2 L^{\text{ref}} l_R}{c^2} \ln\left(\frac{L^{\text{ref}}}{l_R}\right) \left[\frac{(h * h)(k_\perp)}{h(k_\perp)}\right]^2 \ll 1, \tag{5.7}$$

where $h(k_\perp)$ is the input turbulence spectrum.

The additional convolution term

$$\Gamma = \left[\frac{(h * h)(k_\perp)}{h(k_\perp)}\right] \tag{5.8}$$

can be calculated numerically for different synthetic spectra. Figure 5.1 shows Γ for a white spectrum with $h(k_\perp) = 1$ for $|k_\perp| < 21\,\text{cm}^{-1}$, a Kolmogorov-like spectrum with $\eta_1 = 0$, $\eta_2 = 2$ and $k_{\text{knee}} = 5\,\text{cm}^{-1}$ and for a Gaussian spectrum cf. 4.5 with $l_{\min} = l_{\max} = 0.3\,\text{cm}$ and $\beta = 0°$. All assumed spectra are symmetric to $k_\perp = 0\,\text{cm}^{-1}$. For the white spectrum, the additional Γ reduces the non-linearity factor of normal incidence since the convolution of two top-hat functions yields a triangular shape. For more realistic Kolmogorov-like and Gaussian spectra that exhibit spectral decay, Γ increases, especially for higher wavenumbers. This can greatly reduce the critical turbulence level that marks the transition to the nonlinear regime.

5.2 2D full-wave simulations

Realistic fusion plasmas can have high fluctuation levels ($> 5\%$) and fast varying plasma parameters. Thus, i.e. multi-reflections, wave trapping and frequency mixing can occur, such that the Born approximation will not describe the plasma-wave

5. Doppler reflectometry modeling

interaction properly. Time-dependent full-wave methods that give direct solutions to the Maxwell equations, have to be used.

In this thesis, the *Finite-Difference Time Domain* method based full-wave code IPF-FD3D [33] developed at the IGVP Stuttgart is used. The code simulates the propagation and scattering of the electromagnetic beam in two or three dimensions. In this work, the two-dimensional version has been employed.

The plasma is modeled by the electron equation of motion for the plasma current J in the cold plasma approximation

$$\frac{\partial}{\partial t}J = \epsilon_0 \omega_{pe}^2 E - \omega_{ce} J \times \hat{B}_0. \tag{5.9}$$

The background density and magnetic field are included via the plasma frequency ω_{pe} and the electron cyclotron frequency ω_{ce}, that were already introduced in (3.4). $\hat{B}_0$ is the unity vector in direction of the background magnetic field B_0. Together with the two Maxwell equations for the electric and the magnetic field

$$\frac{\partial}{\partial t}E = \frac{1}{\epsilon_0}\nabla \times H - \frac{1}{\epsilon_0}J, \tag{5.10}$$

$$\frac{\partial}{\partial t}H = -\frac{1}{\mu_0}\nabla \times E, \tag{5.11}$$
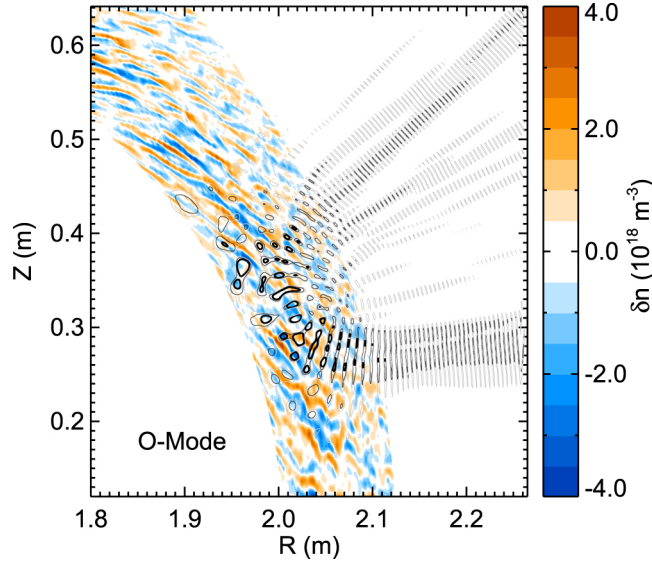
the three equations (5.9)-(5.11) build a complete system. Thus, this approach computes all components of the wave and is therefore called full-wave analysis.

The partial differential equations are implemented as finite difference equations on a spatial Cartesian Yee grid [34]. This method addresses the dependence of the electric and magnetic field due to the curl in Maxwell's equations. It uses two staggered grids, one for the magnetic field and one for the electric field and the current, displaced by half a grid step. A temporal leapfrog scheme is applied. The electron response (5.9) is integrated separately using a modified Crank-Nicolson method.

The input to the simulation is a spatial array of the background density and the background magnetic field in three components B_t, B_r, and B_z. The reflectometer antennas are modeled by fundamental Gaussian beams positioned at the edge of the plasma grid. The irradiation angles θ are defined with respect to the R-axis. The simulation is able to probe with multiple frequencies at once. To ensure sufficiently refined time stepping, the length of a simulation time step Δt is determined by a reference frequency that is larger than any probing frequency. For signal discrimination all frequencies that are used need to be integer multiples of a constant frequency step Δf, here 50 MHz and 200 MHz for X- and O-mode, respectively.

The output signal of the simulation is a complex heterodyne signal at the antenna position, like obtained in the experiment. The simulation must run for a sufficiently long time to capture all scattering effects of the waves. To obtain a time-dependent signal, the simulation is run on successive turbulence frames. For each frame *frozen turbulence* is assumed, since the time scale of turbulent density changes (μs) is much larger than the wave propagation time (ns).

28

Figure 5.2: Full-wave simulation on gyrokinetic turbulence simulation using GENE. The black contours represent the waves electric field. More dark contours correspond to a stronger electric field. (adapted from [7])

A simulation setup using IPF-FD3D is shown in figure 5.2. It shows the propagated electric field as black contours on the density field obtained from gyrokinetic turbulence simulations using the code GENE [26]. The antenna is placed at $(R, z) = (2.265, 0.3)$ m. The contours show the wave's propagation, reflection and back-scattering at its cut-off. At the scattering region near the turning point, where the contours get stronger, the electric field reaches a maximum.

5.3 Impact of the density wavenumber spectrum on the perpendicular velocity measurement

Since the probing beams in Doppler reflectometry are Gaussian with a certain beam waist w_0, the wavenumber range detected by the reflectometer is also Gaussian with a width Δk. Consequently, this will affect the back-scattered signal as the fluctuation power depends on the wavenumber. The effect can be captured by convolution $C(k)$ of the probing beam with the turbulence spectrum. Considering the convolution theorem, this results in a multiplication in Fourier space

$$C_{k_\perp}(k) = h(k)G_{k_\perp}(k). \tag{5.12}$$

Here, $G_{k_\perp}(k)$ is the Gaussian beam field distribution

$$G_{k_\perp}(k) = e^{\frac{-(k-k_\perp)^2}{2\Delta k^2}}, \tag{5.13}$$

where $k_\perp$ is the dominant wavenumber and Δk the spectral resolution, which can be obtained using equation (3.14) or the weighting function method presented in section 3.3.

5. Doppler reflectometry modeling

Thus, a decaying density wavenumber spectrum, such as a Kolmogorov-like spectrum cf. (4.1) strongly affects the convolution (5.12) and thereby the back-scattered signal. It deforms the original Gaussian beam distribution and displaces the maximum towards a smaller wavenumber $k_{\perp,\text{conv}}$. The main back-scattered signal thus corresponds to a lower wavenumber than initially probed. Since the perpendicular velocity is directly related to the wavenumber $v_\perp = \omega_D/k_\perp$, this also affects the determination of the velocity. For density fluctuations moving with $v_{\perp,\text{in}}$ a velocity

$$v_{\perp,\text{exp}} = X \cdot v_{\perp,\text{in}}, \tag{5.14}$$

is expected to be measured, where $X = k_{\perp,\text{conv}}/k_\perp$.

The scaling factor X can be obtained analytically by evaluating (5.12) and determining the maximum's wavenumber $k_{\perp,\text{conv}}$ that satisfies

$$\frac{\partial C_{k_\perp}(k)}{\partial k} = 0. \tag{5.15}$$

For a Kolmogorov-like turbulent wavenumber spectrum with a spectral decay

$$h(k) = k^{-\eta}, \tag{5.16}$$

solving (5.15) results in a maximum at:

$$k_{\perp,\text{conv}} = \frac{k_\perp + \sqrt{k_\perp^2 - 4\eta\Delta k^2}}{2}. \tag{5.17}$$

Thus, the scaling factor in (5.14) is

$$X = \frac{k_{\perp,\text{conv}}}{k_\perp} = \frac{1}{2} + \sqrt{\frac{1}{4} - \eta\frac{\Delta k^2}{k_\perp^2}} < 1. \tag{5.18}$$

Analytic results for $\eta = 0$, $\eta = 1$ and $\eta = 2$ are shown in figure 5.3(a) in blue. The corresponding spectral resolution is shown in figure 5.4. It is computed using (3.14) assuming $R_b = 0.2\,\text{m}$, $\theta = 10°$ and $w_0 = 22\,\text{mm}$ in a circular geometry with $R_c = 0.4\,\text{m}$. For a white turbulence spectrum where the spectral index $\eta = 0$, there is no difference between the probed wavenumber and the mainly back-scattered wavenumber. If $\eta > 0$, large deviations up to 30% can be expected for small wavenumbers. Results for a Kolmogorov-like spectrum, with $\eta_1 = 0$, $\eta_2 = 2$, $k_{\text{knee}} = 5\,\text{cm}^{-1}$ is shown in red. The data points were calculated numerically to capture the jump due to the spectral knee. However, for more realistic spectra, where $\eta > 0$ for $k < k_{\text{knee}}$, a smaller jump but also larger deviations at small wavenumbers can be expected.

Note that this also results in a condition for the calculation:

$$k_\perp^2 - 4\eta\Delta k^2 > 0. \tag{5.19}$$

Thus, in a certain parameter range, where the probed wavenumber is small and the spectral width Δk is usually large, no maximum can be determined and the measured velocity can not be defined.
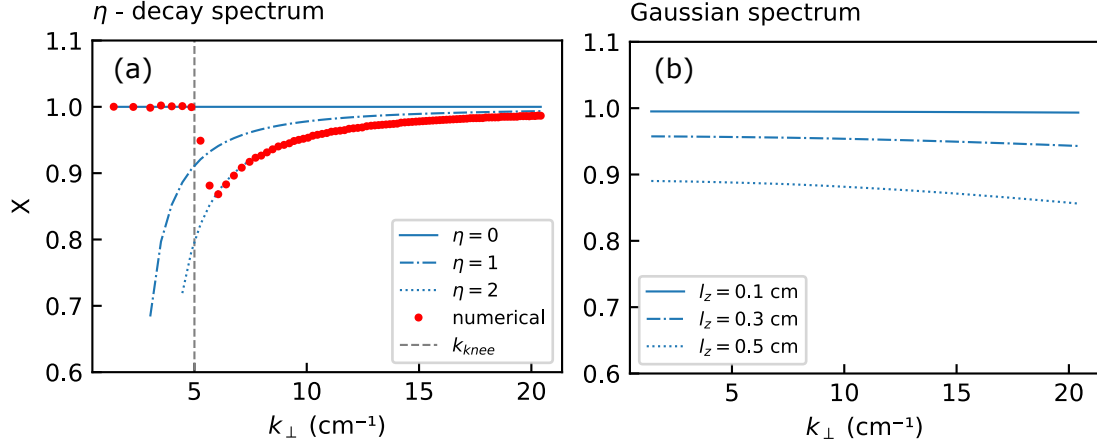
Figure 5.3: Scaling factor X cf. (5.14) for different turbulence spectra. The used spectral resolution is shown in figure 5.4. (a) Analytic results of η-decay spectrum error (5.17) for different η (blue) and numerical result for a Kolmogorov-like spectrum with $\eta_1 = 0$, $\eta_2 = 2$ and $k_{\mathrm{knee}} = 5$ cm^{-1} (red). (b) Analytic results for Gaussian spectrum (5.21) for different correlation lengths l_z.
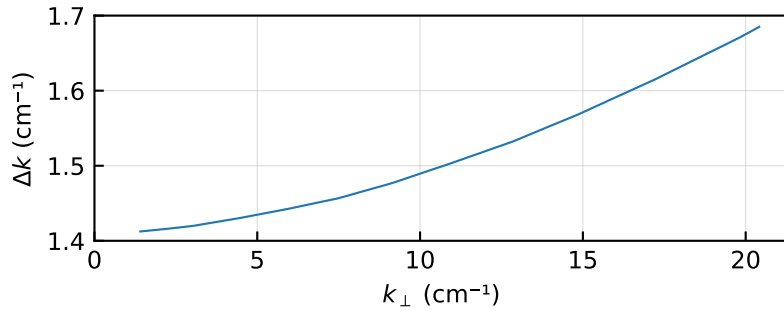
Figure 5.4: Spectral resolution (3.14) for different wavenumbers, that is used for figure 5.3. $R_c = 0.4$ m, $R_b = 0.2$ m, $w_0 = 22$ mm and $\theta = 10°$ are kept constant.

5. Doppler reflectometry modeling

A similar expression can be obtained for the Gaussian turbulence spectrum. From equation (4.5) it can be derived that

$$h(k_z) = \frac{l_z}{\sqrt{8\pi}} \exp\left[-l_z^2 k_z^2/8\right],$$
(5.20)

where l_z is the correlation length in z-direction. Then, the resulting scaling factor is

$$X = \left[1 + \frac{\Delta k^2 \, l_z^2}{4}\right]^{-1},$$
(5.21)

which is shown in figure 5.3(b) for several correlation lengths l_z. In contrast to the η-decay the scaling factor is not directly dependent on the probed wavenumber $k_\perp$. The error increases for higher wavenumbers due to the spectral resolution Δk only. For slab geometry where the spectral resolution cf. (6.1) is constant also X will be constant.

6 Simulation results using synthetic turbulence

Recent research is concerned with the occurrence of poloidal asymmetries in the measurement of the perpendicular velocity [8, 9, 10, 11]. The measured perpendicular velocity was found to depend on the poloidal measurement position in some, but not all, experiments. The reason for the occurrence of these deviations is not yet completely understood and a diagnostic effect cannot be excluded. The use of methods such as full-wave simulations is therefore essential for a better understanding of the diagnostic response by taking into account all types of plasma-wave interactions during the simulation. Previous perpendicular velocity studies using full-wave methods have already been presented in [35].

For studies focusing on one specific turbulence feature, synthetic turbulence as presented in chapter 4 is particularly suitable. Turbulence patterns of isotropic and anisotropic turbulence spectra can rapidly be generated and varied. Perpendicular velocities can be investigated in different geometries by shifting the pattern. Realistic poloidal plasma shapes, such as the D-shape at AUG, are approximated using a straight *slab geometry* and a *circular geometry*. For the latter, the radius of curvature of the plasma is also taken into account. The perpendicular velocity is implemented as a constant bulk velocity that can directly be compared to the simulation result. Clearly, full-wave analysis of gyrokinetic turbulence simulations will be of great use in the future, as it accounts for the complexity of realistic turbulence in its entirety. However, this is beyond the scope of this thesis. Preliminary results are discussed in the outlook 7.2.

After presenting the input geometries used and the simulation setup, this chapter presents the results on synthetic turbulence with constant velocity. The velocity measurements are investigated with respect to non-linear scattering regimes, different turbulence spectra, variation of the antenna position and anisotropic structures.

6.1 Plasma modeling and simulation setup

The background plasma profiles of electron density n_e and magnetic field B are shown in figures 6.1(a) and 6.1(b), respectively. Only the toroidal field B_t is shown as the others are set to zero, since usually $B_r, B_\theta \ll B_t$. They are adapted from the midplane of AUG shot #31260, which was already investigated regarding non-linearities in the back-scattered power using full-wave analysis [7, 6].

For the simulations two different geometries are used. One of them, is the so-called

6. Simulation results using synthetic turbulence
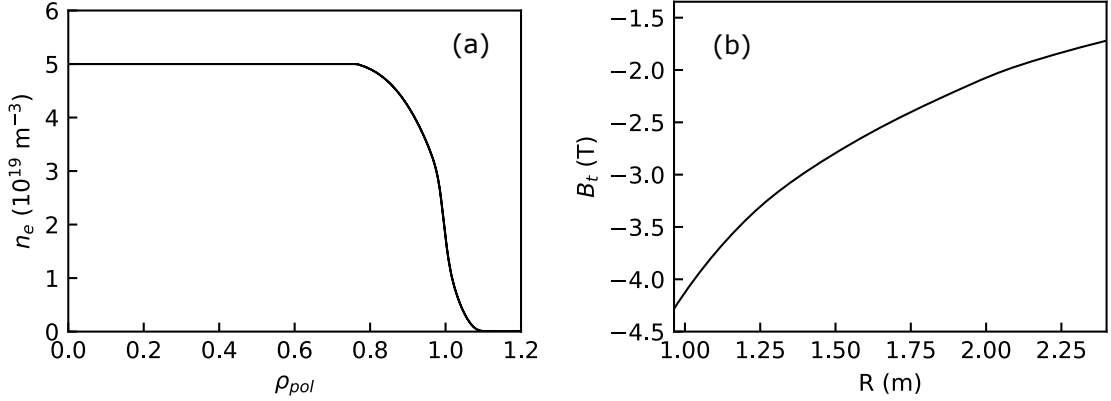
Figure 6.1: (a) Background density profile $n_e(\rho_{pol})$ and (b) background magnetic field profile $B_t(R)$, adapted from AUG # 31260.

slab geometry. Here, the radius of curvature is assumed to approximate $R_c = \infty$ so that the refractive index layers are completely flat. This geometry significantly simplifies the physical problem an thus makes the formulation and comparison to analytical predictions much easier. The slab geometry is presented in the density contour plot 6.2(a). Therefore, n_e and B_t from figure 6.1 are elongated along the z-axis, remaining constant along R. To account for more realistic plasma shapes, curvature must be considered by using a *circular geometry*. Therefore, the density n_e on the midplane is rotated about the center. The obtained density contour is shown in figure 6.3(a). B_t is stretched along z similar to the slab geometry.

Figures 6.2(b) and 6.3(b) show the simulation grids for both geometries that are used in the following simulations. The plots show contours of ρ_{pol} the X-mode cut-off frequencies $f_{co,X}$ that are obtained using (3.7). The O-mode cut-off contours are not shown since they are aligned with the poloidal magnetic flux surfaces. The antenna positions are marked in both figures in black. They are at $(R, z) = (2.3, 0.3)$ m for the slab geometry and on the midplane at $(R, z) = (2.3, 0.0)$ m for the circular geometry. The Gaussian beams have a waist of $w_0 = 22$ mm and are directed upwards. Exemplary rays are indicated in for O-mode and X-mode. Wavenumbers $k_\perp = 2 - 20$ cm^{-1} are probed with frequencies $f_O = 58 - 77$ GHz, $f_X = 92 - 98$ GHz using injection angles in a range of $\theta = 0 - 25°$.

The turning points of O-mode and X-mode simulations are shown in blue and red, respectively. Frequencies and angles are optimized such that they approach $\rho_{pol} = 0.9$ using a raytracing code similar to TORBEAM [36]. Thus, the plasma curvature radius is approximately $R_c = 0.4$ m for circular geometry at poloidal flux surface of interest. AUG plasmas have usually a higher curvature radius of approximately $R_c = 0.75$ m. An increase in the curvature radius will of course decrease the spectral resolution regarding (3.14). Nevertheless, this still represents curvature radii of smaller experiments.
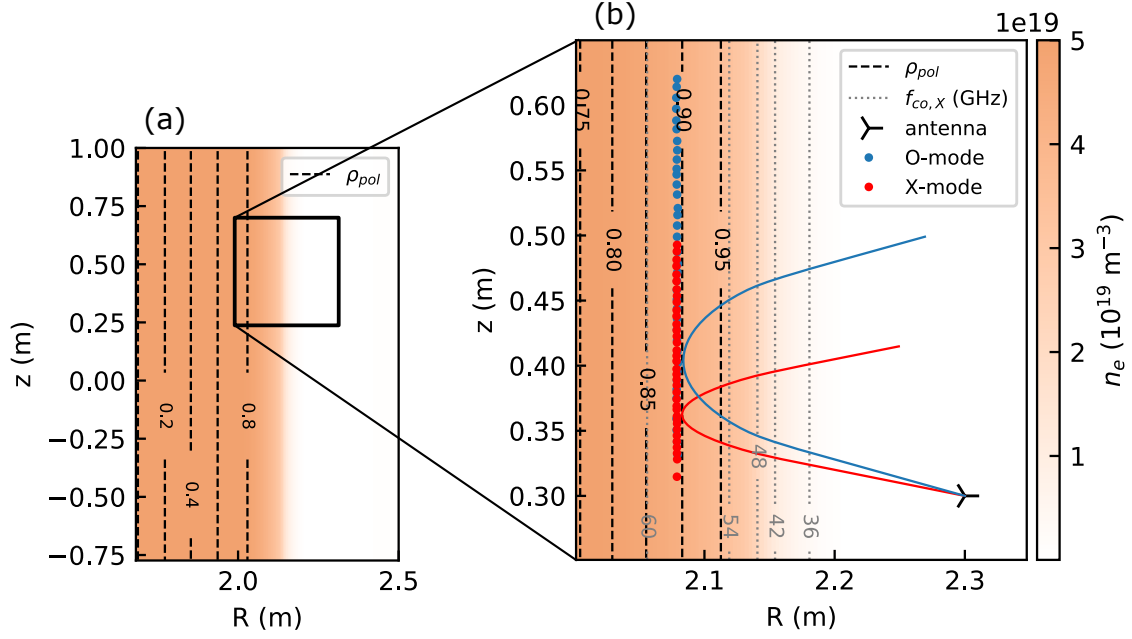
Figure 6.2: (a) Full slab geometry and (b) the simulation domain. The turning points and exemplary beam paths, that are determined using raytracing are shown for O-mode (blue) and X-mode (red). The antenna is at $(R, z) = (2.3, 0.3)$ m.
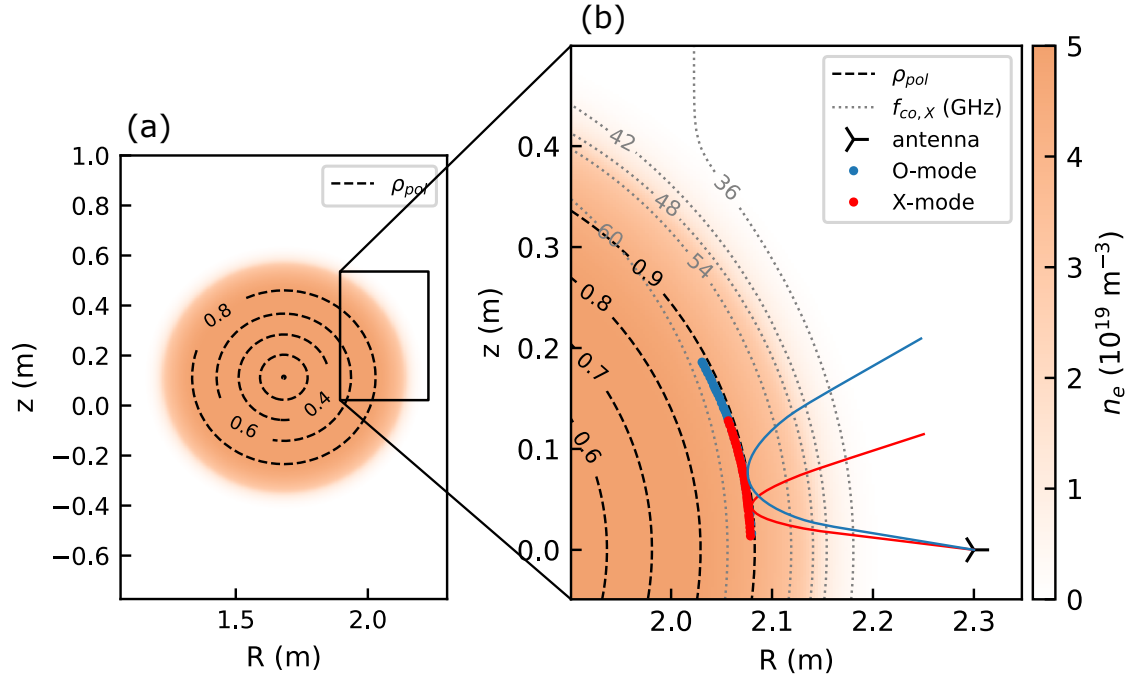
Figure 6.3: (a) Full circular geometry and (b) the simulation domain. The turning points and exemplary beam paths, that are determined using raytracing are shown for O-mode (blue) and X-mode (red). The antenna is at $(R, z) = (2.3, 0.0)$ m.
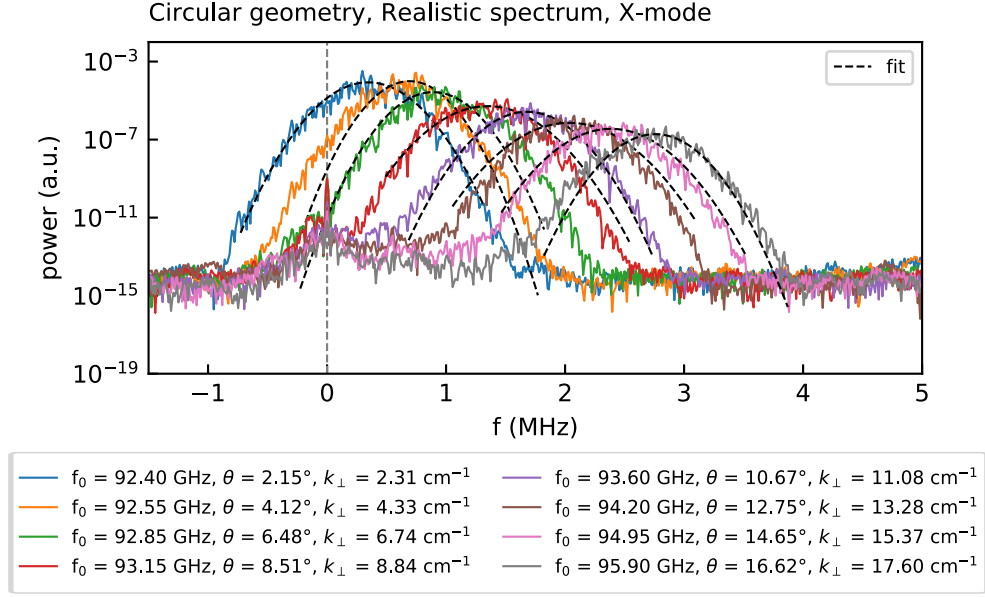
Figure 6.4: Exemplary Doppler spectra output using the full-wave analysis. The data is obtained for the realistic turbulence wavenumber spectrum (cf. section 6.2.2) in circular geometry using X-mode probing at $\rho_{pol} = 0.9$.

The propagation velocity of density fluctuations is fixed at $10\,\text{km/s}$ for all simulations. This is in an order of magnitude that is normally measured in fusion experiments. However, the velocity is completely independent of the simulation and it is only used in the signal analysis. To obtain the Doppler spectrum, a $\Delta t = \Delta z / v_{\perp}$ between the turbulence frames is required in the Fast-Fourier Transform. In this work, the turbulence pattern is shifted by $\Delta z = 0.001\,\text{m}$ at each forwarding. The time step size is thus $\Delta t = 1 \times 10^{-7}\,\text{s}$, resulting in a maximum frequency of $f_{\max} = 1/(2\Delta t) = 5\,\text{MHz}$ in the Doppler spectrum. This is sufficient to fully map all Doppler peaks.

Typical Doppler shifted spectra that are obtained from the full-wave simulation are shown in figure 6.4 for a realistic turbulence spectrum with $\eta_1 = 0$, $\eta_2 = 2$, $k_{\text{knee}} = 5\,\text{cm}^{-1}$. The data is obtained in circular geometry using X-mode. Similar to the analysis presented in chapter 3, the back-scattered powers P and perpendicular velocities $v_{\perp}$ can be obtained using Gaussian fits. In the figure, the fits are indicated dashed black. All spectra clearly show a Doppler shift that increases with the probed wavenumber. For the wavenumbers $k_{\perp} < k_{\text{knee}}$ (blue and orange line), where the turbulence spectrum is assumed to be constant, the approximately same power is obtained. For larger wavenumbers, the power steadily decreases with increasing the wavenumber, which already indicates the decay in the density wavenumber spectrum.

6.2 Investigations of diagnostic effects in perpendicular velocity measurements

6.2.1 Turbulence level

Previous studies have shown that high turbulence levels can significantly affect the scattering of electromagnetic waves in reflectometry experiments [6, 7, 25]. With an increasing turbulence level, multiple scattering events can lead to an increase of the back-scattered power, so that (3.9) loses its validity. The transition to nonlinear scattering can be estimated theoretically with the γ factor (5.7), which could be confirmed through experimental and full-wave results.

The effect of higher turbulence levels on the perpendicular velocity has already been studied in theory [37]. An influence on the measured velocity is not expected in homogeneous plasmas. Full-wave results, using slab geometry, could confirm this for turbulence levels up to 10% [35].

Increasing turbulence levels are studied for slab geometry using X-mode polarization. A Kolmogorov-like turbulence spectra with $\eta_1 = 0$, $\eta_2 = 2$, $k_{\text{knee}} = 5 \, \text{cm}^{-1}$ is used. The turbulence pattern is shifted only 40 times by Δz. Thus, only a resolution of $\Delta f = 0.1 \, \text{MHz}$ is obtained in the Doppler spectrum. Figures 6.5(a) and 6.5(b) show the back-scattered power P and the obtained velocity $v_\perp$ plotted against the turbulence level $\delta n / n_0$, respectively.

As a reference, a linear power response cf. (3.9) is indicated dashed black in the power response results in fig. 6.5(a). It shows, that even for this low resolution simulations the power response is linear until it reaches turbulence levels of $\delta n / n_0 > 1\%$. At higher turbulence levels, the back-scattered power saturates. This confirms other studies using the physical optics model [32] and full-wave simulations [32, 6]. Usually, however an enhanced response due to multiple scattering events, is observed before saturation occurs. This is probably not visible in the results here due to the low frequency resolution.

The obtained perpendicular velocities in fig. 6.5(b) are all around the input velocity. In between the different probed wavenumbers, slight deviations are to be expected due to the underlying turbulence spectrum and the probing beam width, as discussed in section 5.3. The perpendicular velocities for a fixed probed wavenumber show no significant variation when increasing the turbulence level. First small deviations are observed when applying turbulence levels $\delta n / n_0 > 1\%$.

In the following, no correlation between the γ factor for the reflectometer power response and a diagnostic effect on the perpendicular velocity measurement is assumed.

6.2.2 Isotropic turbulence wavenumber spectra

Simulations for several different isotropic turbulence spectra are performed to investigate further effects on the velocity measurement. The investigated turbulence

6. Simulation results using synthetic turbulence
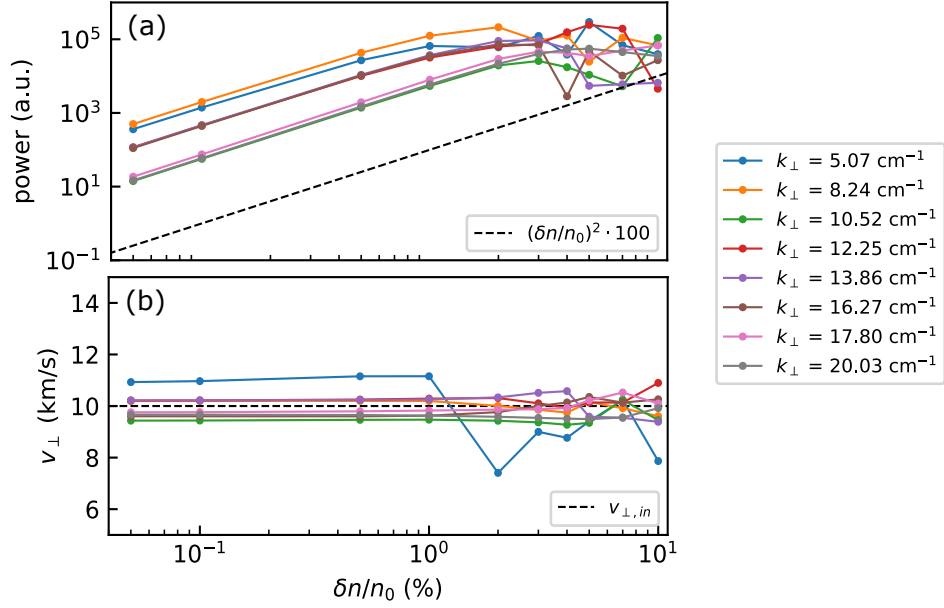
Figure 6.5: Analysis of nonlinear effects in (a) the power response and (b) the perpendicular velocity measurement using full-wave simulations. The results are obtained in slab geometry using X-mode probing, for only 40 turbulence frames. The power response shows linear response for $\delta n/n_0 < 1\%$. The perpendicular velocities are not much affected by the turbulence level.

spectra with isotropic turbulence are:

- **White spectrum:** $h(k) = 1$ for $0 \leq k \leq 21$ cm^{-1},

- **Gaussian spectrum:** $h(k) =$ eq. (4.5) with $l_{\min} = l_{\max} = 0.3$ cm, $\beta = 0°$,

- **Realistic spectrum:** $h(k) =$ eq. (4.1) with $\eta_1 = 0, \eta_2 = 2, k_{\mathrm{knee}} = 5$ cm^{-1}.

The correlation lengths are determined numerically as described in section 4.1.3 and are listed in table 6.1. The correlation length of the Gaussian spectrum can be confirmed. Since the white spectrum does not undergo spectral decay, it contains more smaller structures and its correlation length is significantly smaller.

All simulations are performed with a turbulence level of $\delta n/n_0 = 0.1\%$. The nonlinearity factors γ for the different turbulence spectra are determined using (5.7) and are shown in figure 6.6. For the O-mode, no deviations in the measured power spectrum are expected. For the X-mode, the Gaussian and the realistic spectrum measurements are already performed for $\gamma > 1$ at higher probed wavenumbers. This could lead to more back-scattered power due to multiple scattering. The previous results in section 6.2.1 have shown that no deviation in the velocity is expected even in the nonlinear regime. However, as discussed in section 5.3, deviations caused by the probing beam width are to be expected. Furthermore, they will strongly depend on the underlying turbulence spectrum.

	l_R (in cm)	l_z (in cm)
White	0.086 ± 0.001	0.088 ± 0.003
Gaussian	0.29 ± 0.05	0.31 ± 0.02
Realistic	0.34 ± 0.01	0.35 ± 0.02

Table 6.1: Correlation lengths for all three turbulence spectra presented in section 6.2.2. The correlation lengths are computed numerically as described in section 4.1.3.
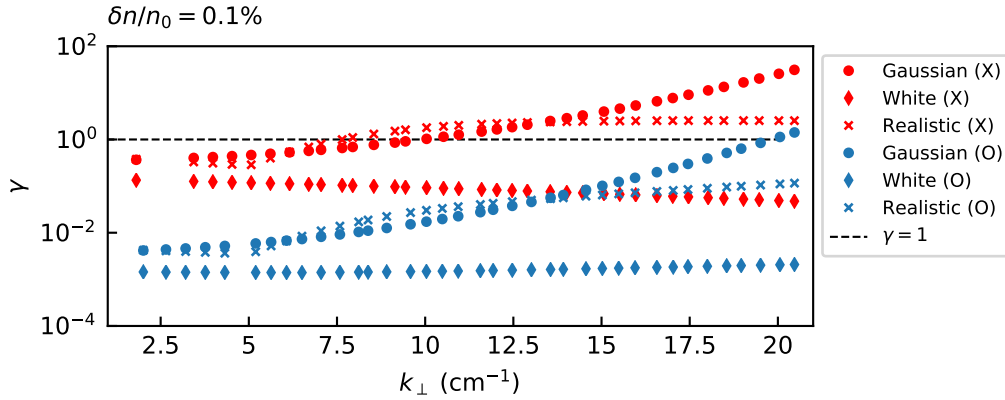
Figure 6.6: Non-linearity factor γ cf. equation (5.7) for $\delta n/n_0 = 0.1\%$ in circular geometry. The data points correspond to the turning points in figure 6.3, respectively. The O-mode probing is almost completely in the linear regime for all spectra. The X-mode probing for the Gaussian spectrum and the realistic spectrum enters the nonlinear regime for higher wavenumbers.

The results of the full-wave simulations on the three different spectra are presented for slab geometry in figure 6.7. The obtained turbulence wavenumber spectra are shown on the left side. There, the input spectra are shown in gray. They are arbitrarily scaled so that the spectra can easily be compared with the full-wave results. Note that, since $P \propto h^2(k)$ for the realistic spectrum $\alpha = \eta^2$ is the expected spectral decay. The direct simulation results P are shown in the dark colors for O-mode in blue and for X-mode in red. Corresponding fits are included by dashed lines for the white spectrum and the realistic spectrum.

The results for the perpendicular velocities are shown on the right. O-mode and X-mode results in blue and red, respectively. The data points include an uncertainty band, that is mainly due to the spectral resolution Δk that is obtained via (3.14). The input velocity is shown in gray. The velocity $v_{\perp,\mathrm{exp}}$ cf. (5.14) that is expected due to the probing beam width, is shown dashed in the color of the respective polarization. Even if it is hardly visible for slab geometry, the expected velocities vary depending on their polarization, since the probing frequencies f_0 differ decisively.
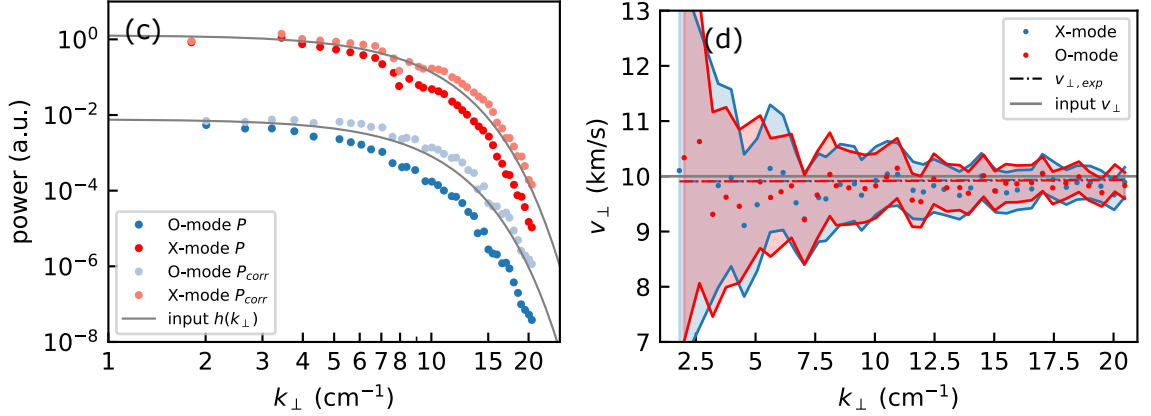
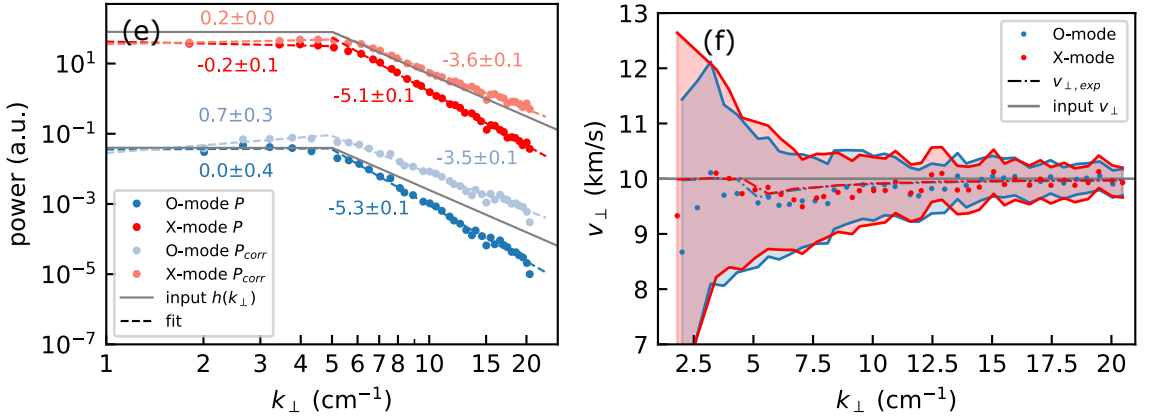# 6. Simulation results using synthetic turbulence

Slab geometry

White spectrum:
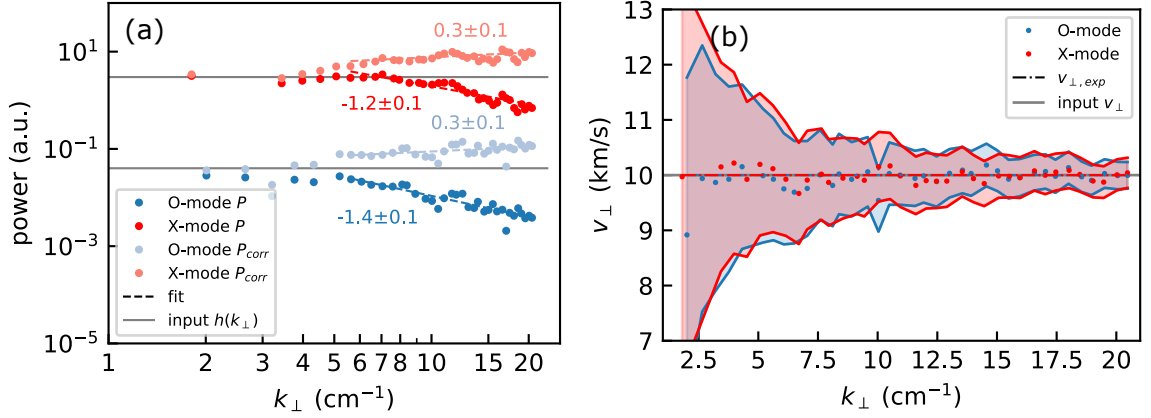
Gaussian spectrum:

Realistic spectrum:

Figure 6.7: Full-wave results of turbulence wavenumber spectrum (a, c, e) and perpendicular velocities (b, d, f) in slab geometry for a white spectrum (a, b), a Gaussian spectrum (c, d) and a realistic Kolmogorov-like spectrum (e, f). The results for O-mode and X-mode are shown in blue and red, respectively. The spectra include direct P and corrected P_{corr} power results. The perpendicular velocities are compared to the expected velocity $v_{\perp,\text{exp}}$ due to the probing beam width. For more details refer to the text.

Particularly striking for all obtained density wavenumber spectra 6.7(a, c, e) is the consistently too steep spectral decay for large wavenumbers $k_\perp > 5$ cm^{-1}. The deviation is especially evident for the white spectrum 6.7(a) where no decay is expected. This effect was already observed in 2D full-wave simulations [32, 33, 35] and can be explained by the so-called *scattering efficiency* . It takes into account that the actual scattering region is not perfectly aligned with the cut-off, as it can be studied in detail using the weighting function as shown in figure 3.3(b). The resulting error can be corrected by [32]

$$P_{\text{corr}} = P \left[1 + \left(\frac{L^{\text{ref}}}{8k_0^2} \right)^{2/3} k_\perp^2 \right], \tag{6.1}$$

where L^{ref} is the refractive index scale length, $k_0 = 2\pi f_0/c$ is the vacuum wavenumber, $k_\perp$ is the probed wavenumber and P is the initially obtained back-scattered power. Equation (6.1) is deduced solving the Helmholtz equation in slab geometry analytically using O-mode polarization cf. equation (5.1) and assuming a linear density profile. Applicability for other geometries and X-mode polarization is achieved due to L^{ref}. The corrected back-scattered power P_{corr} is shown in light colors in all obtained spectra.

For the white spectrum in fig. 6.7(a), the correction (6.1) improves the results, especially for the larger wavenumbers. However, the back-scattered power then increases slightly with the wavenumber. Furthermore, the power measured at smaller wavenumbers, which already fits well without the correction, also increases. Since the study of the white spectrum, cf. figure 6.6, is done in a fully linear regime, an increased power response is not expected. The full-wave results for the Gaussian spectrum in fig. 6.7(c) show similar behavior. The corrected results also appear to be in better agreement, but an undesirable increase is observed at smaller wavenumbers. The realistic spectrum in fig. 6.7(e) is also well captured. The full-wave results show the plateau and spectral decay. The knee position is well defined and at the expected location. The correction agrees better with the input spectrum, although it slightly over-corrects for all wavenumbers.

The perpendicular velocities that are shown in fig. 6.7(b, d, f) are in good agreement with the expected velocity for all spectra. Due to the infinite curvature radius the spectral resolution cf. (3.14) is very good and the expected deviations are consequently small. The velocity for the white spectrum in fig. 6.7(b) is expected not to deviate at all since $\eta = 0$ in eq. (5.17). This could nicely be reproduced by the full-wave simulations. For the Gaussian spectrum, the velocities shown in fig. 6.7(d) expresses the small constant deviation towards lower velocities. The velocity results in fig. 6.7(f) for the realistic spectrum also match very well with the expected velocity. The obtained drop at the knee position can also be seen in the full-wave data.

The results for the circular geometry are shown in figure 6.8. The plots are structured and color-coded in the same way as for the slab geometry.

The density-wavenumber spectra are shown in figures 6.8(a, c, e) on the left. Similar to the slab geometry, all spectra show the slightly over-corrected P_{corr} results.
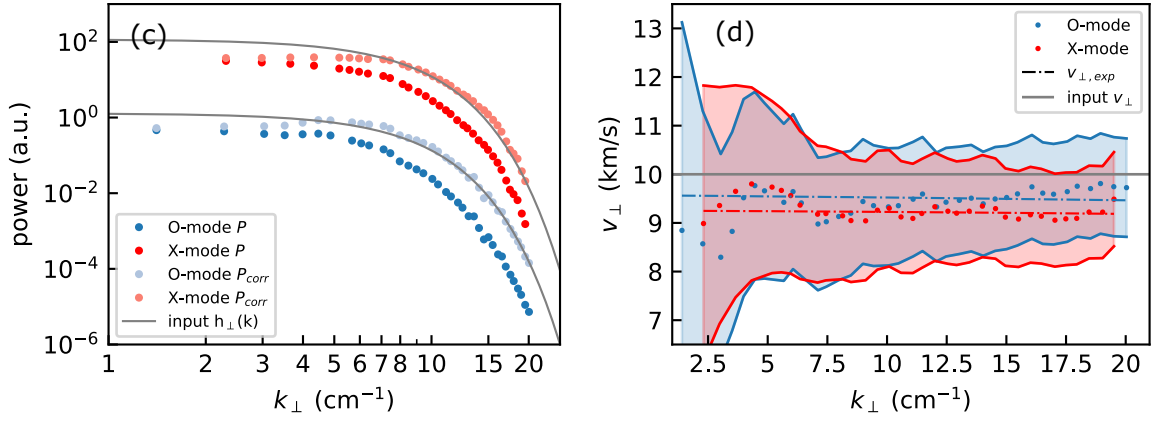
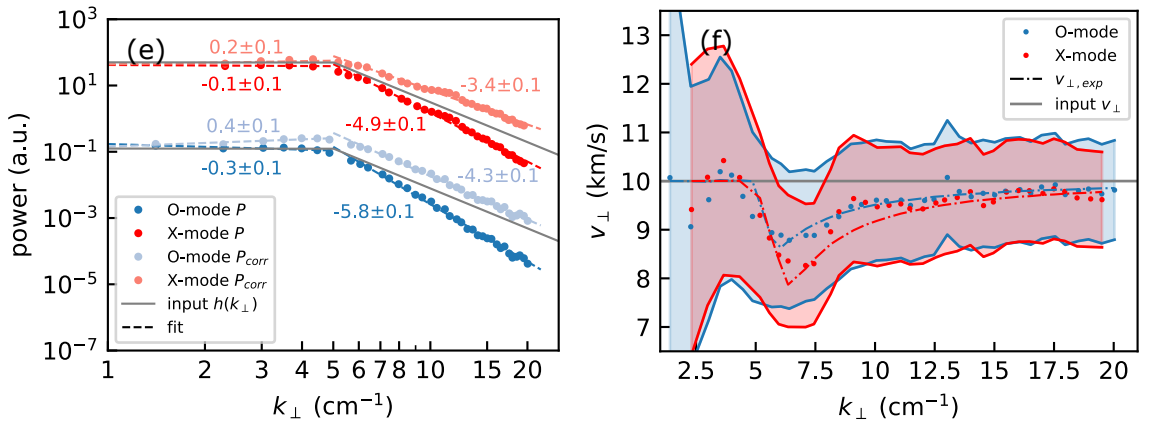*6. Simulation results using synthetic turbulence*

Circular geometry

White spectrum:
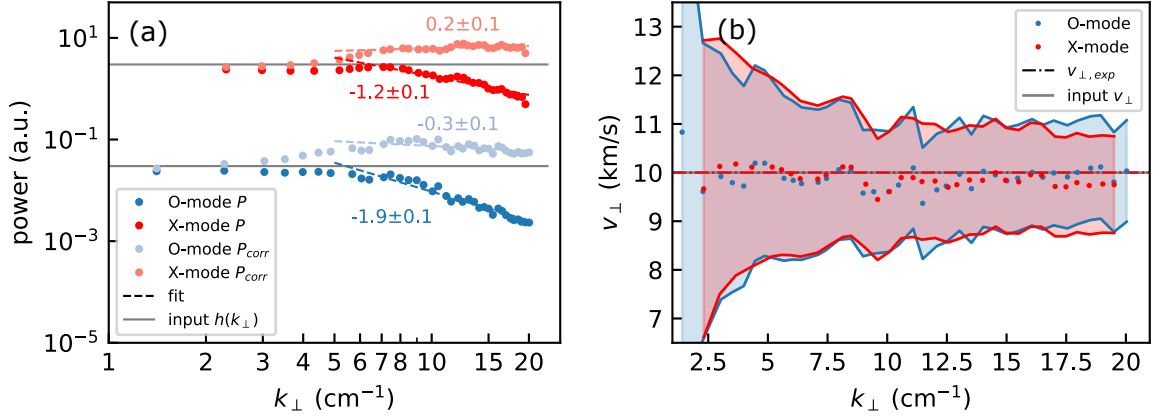
Gaussian spectrum:

Realistic spectrum:

Figure 6.8: Same as figure 6.7 for full-wave simulations in circular geometry. Due to the curvature radius the spectral resolution is lowered. Thus, the uncertainty band of the full-wave perpendicular velocity results (b, d, f) increases. Further, the expected velocity $v_{\perp,\mathrm{exp}}$ and the full-wave results show increased deviations and the difference in between O-mode and X-mode perpendicular velocity results is more pronounced.

Nevertheless, they lead to better accordance with the input spectra. It should be emphasized that again the knee position can be captured well in the realistic spectrum in fig. 6.8(e).

The results for the perpendicular velocities are shown on the right-hand side in figures 6.8(b, d, f). Due to the plasma curvature, the spectral resolution Δk cf. (3.14) is significantly decreased compared to the spectral resolution in the slab geometry. On the one hand, this leads to an increased uncertainty in the velocity and, on the other hand, to an increased deviation to be expected due to the probing beam width. Furthermore, the expected differences in O-mode and X-mode $v_{\perp,\text{exp}}$ get more pronounced.

The full-wave results clearly show no deviation for the white spectrum in fig. 6.8(b) and thus confirm the expected velocity. For the Gaussian spectrum in fig. 6.8(d), deviations of different magnitudes are to be expected depending on the polarization, both of which are almost constant for all wavenumbers. The full-wave results show the two different levels of deviation. However, the slightly better agreement is observed for larger wavenumbers $k_\perp > 10\,\text{cm}^{-1}$. For smaller wavenumbers, there is more variation within the uncertainty band. Exceptionally good agreement is obtained for the realistic spectrum in fig. 6.8(f). It can clearly be seen that the full-wave results show the differently strong drop at the knee position which is to be expected depending on the polarization.

In summary, the density wavenumber spectra, that are obtained with the full-wave simulations, show good agreement with the input spectra. The scattering efficiency correction leads to results that are closer to the input spectra. However, the correction seems to over-correct the results. This is particularly unfavorable for small wavenumbers $k_\perp < 5$ cm^{-1}, where good results are obtained even without the correction. This indicates that the applicability of (6.1) requires further investigation, which is beyond the scope of this thesis.

For all input spectra, the full-wave results of the perpendicular velocities confirm the analytically derived deviations presented in section 5.3. There is a clear dependence of the velocity deviation on the underlying turbulence spectrum, that can lead to deviation in the measured velocity when spectral decays are pronounced. The effect is especially significant for curved plasmas which have a larger uncertainty Δk. Turbulence in fusion plasmas is expected to be Kolmogorov-like and therefore exhibit spectral decay. Furthermore, experimental-like geometries are curved and the spectral resolution is therefore limited (see fig. 3.3(a)). The observed effect can also lead to apparent poloidal asymmetries when the perpendicular velocity is measured on different wavenumbers at different poloidal locations in the plasma. However, the prediction of the deviation always requires the knowledge of the underlying turbulence spectrum. This might be difficult when applied to the experiment. Since the experimental measurement of the turbulence spectrum is also subject to several uncertainties, e.g. non-linear response, a further evaluation regarding the perpendicular velocity might be even more unreliable.
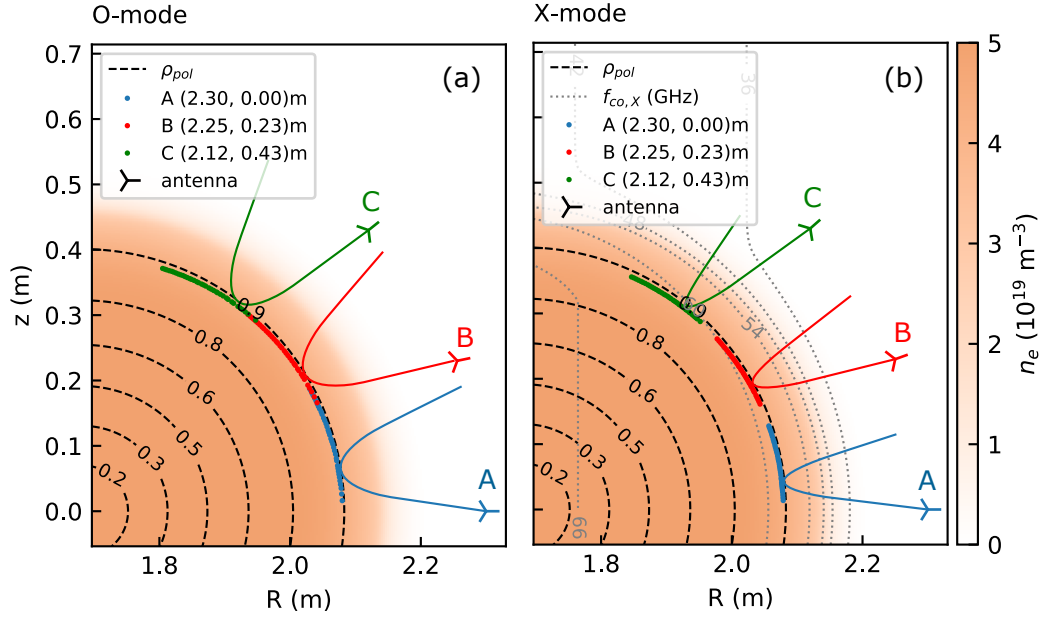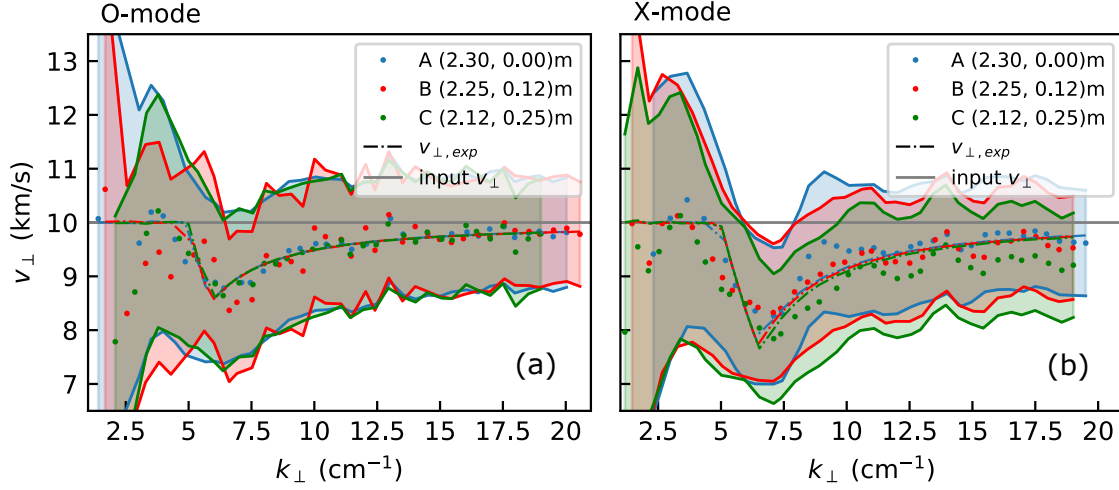
Figure 6.9: The antenna positions and the corresponding turning points for (a) O-mode and (b) X-mode that are used to study diagnostic effects, that depend on the poloidal position of the probing antenna. Exemplary beam paths are shown in the corresponding colors. Poloidal magnetic flux surfaces ρ_{pol} are indicated in dashed black. The X-mode cut-off frequency layers $f_{co,X}$ are shown in (b) in dotted gray.

6.2.3 Poloidal variation of antenna positions

The analysis of different antenna positions aims at effects due to beam propagation on different background. For this reason, the perpendicular velocity results of different antenna locations are compared. The antennas are located at $(R, z)_A = (2.3, 0.0)$m, $(R, z)_B = (2.25, 0.12)$m and $(R, z)_C = (2.12, 0.43)$m. Thereby, they measure at the same distance from the plasma edge. The antenna locations correspond to a poloidal angle of 0°, 22.5° and 45° with respect to the midplane. All antennas are pointed upwards. The antenna positions and the turning points, that are determined using raytracing, are shown in figure 6.9. Exemplary rays are shown for demonstration.

The background magnetic field is indicated by the contours of the X-mode cutoff frequencies $f_{co,X}$. Unlike the O-mode cut-off frequency, which is aligned with the magnetic flux surfaces, these are not symmetric about the plasma center. This originates from the X-mode dispersion relation (3.7), which also depends on the background magnetic field, that varies as a function of R (see fig. 6.1). The dependency is also reflected in the input frequencies f_0 for X-mode that are used for reaching $\rho_{pol} = 0.9$. The more upwards the antenna, the higher the frequencies that are required ($f_{0,A} = 92.4 - 96.8$ GHz, $f_{0,B} = 93.1 - 98.5$ GHz, $f_{0,C} = 95.3 - 101.4$ GHz). Thus, since f_0 is related to the spectral resolution (3.14) a variation of the antenna position might lead to stronger deviations due to the probing beam width. For O-

Figure 6.10: Full-wave results of the perpendicular velocity with a corresponding uncertainty band for a poloidal variation of the antenna position for (a) O-mode and (b) X-mode. The realistic spectrum cf. section 6.2.2 is used. Corresponding antenna positions and turning points are shown in figure 6.9. The expected deviation due to the probing beam width $v_{\perp,\mathrm{exp}}$ is shown dashed in matching colors. While the O-mode results do not differ at all, the X-mode results slightly tend to decrease for varying the antenna position more upwards.

mode the same frequency range can be applied for all antennas, so that no further deviation is to be expected.

The turbulence is modeled using the realistic turbulence spectrum, that is introduced in section 6.2.2. The simulations are performed using a turbulence level of $\delta n / n_0 = 0.1\%$.

The obtained results are shown in figure 6.10(a) and 6.10(b) for O-mode and X-mode, respectively. Each plot includes the full-wave results for the perpendicular velocities from all three antennas, color-coded according to figure 6.9. The input velocity is shown in gray. The expected velocities $v_{\perp,\mathrm{exp}}$ due to the probing beam width are indicated dashed.

Both O-mode and X-mode results show good agreement with the expected velocity for all antenna positions. The differently pronounced drops with respect to the used polarization, cf. figure 6.8(f), can be confirmed. The O-mode results are in perfect agreement within the different antenna positions. The velocities measured in X-mode decrease slightly as one approaches further poloidally. However, the analytical expected velocities, which take into account the changing input frequencies, predict much less pronounced differences. Therefore, another diagnostic effect cannot be excluded. Nevertheless, the deviations are only small. According to the observed trend, more significant deviations would correspond to antennas that are directed even further upwards than antenna C. To measure there, the beams would have to be radiated almost parallel to the cut-off contours, so that corresponding
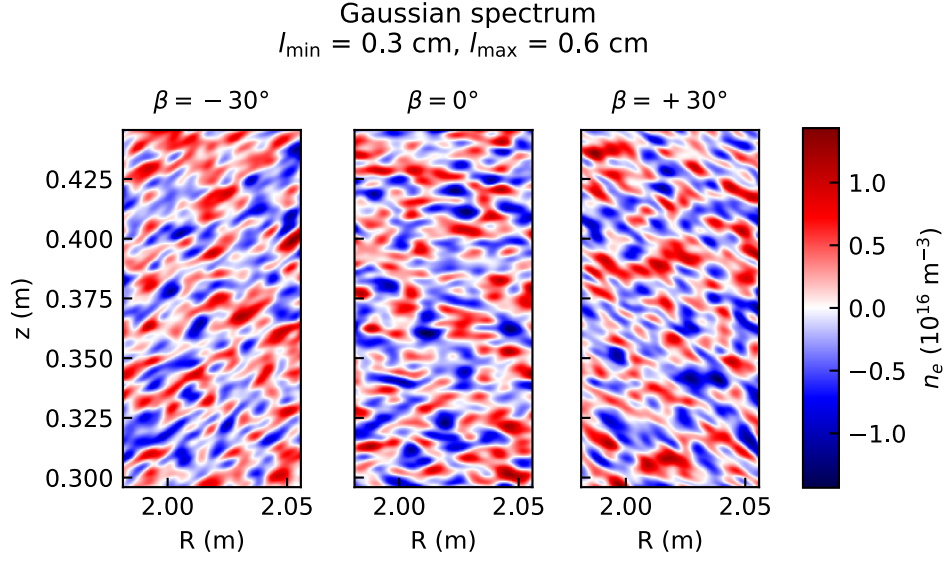
Figure 6.11: Turbulence pattern, that are generated using (4.5) with $l_{\min} = 0.3\,\text{cm}$ and $l_{\max} = 0.6\,\text{cm}$. The turbulence pattern are used to studying anisotropic turbulence structures. Tilt angles of $\beta = 0, \pm 30°$ are investigated in slab geometry.

results would not be meaningful.

No further significant deviations can be observed. Strong poloidal asymmetries that originate from differing antenna positions can be excluded.

6.2.4 Anisotropic turbulence

Realistic turbulence usually exhibits anisotropic structures due to sheared flows. These can also be investigated with synthetic diagnostics using the Gaussian spectrum cf. (4.5). As already discussed in chapter 4, the circular geometry cannot be used here because the velocity is modeled by rotation with respect to the plasma center. Therefore, the tilt angle rotates with and changes with respect to the antenna. For this reason, the influence of anisotropic turbulence on the perpendicular velocity measurement is studied in slab geometry only.

Three different spectra are examined corresponding to three different tilt angles. The used turbulence patterns are shown in figure 6.11. Tilt angles β of 0°, 30° and -30° are used. The turbulence structures are elongated using $l_{\min} = 0.3\,\text{cm}$ and $l_{\max} = 0.6\,\text{cm}$, which are the correlation lengths l_z and l_R, respectively, when there is no tilting. As sketched in figure 4.3(a), a tilt leads to a change in the correlation length. The correlation lengths corresponding to the differently tilted structures are listed in table 6.2.

This also affects the transition to the nonlinear scattering regime. The results for the γ cf. (5.7) are shown in figure 6.12. A turbulence level of $\delta n/n_0 = 0.01\%$ is used. Due to the increased correlation length, tilting of the structures leads to an increase

	l_R (in cm)	l_z (in cm)
$\beta = 0°$	0.60 ± 0.02	0.32 ± 0.04
$\beta = \pm 30°$	0.54 ± 0.02	0.42 ± 0.03

Table 6.2: Correlation lengths for all three turbulence pattern, that are shown in figure 6.11. The correlation lengths are computed numerically as described in section 4.1.3.
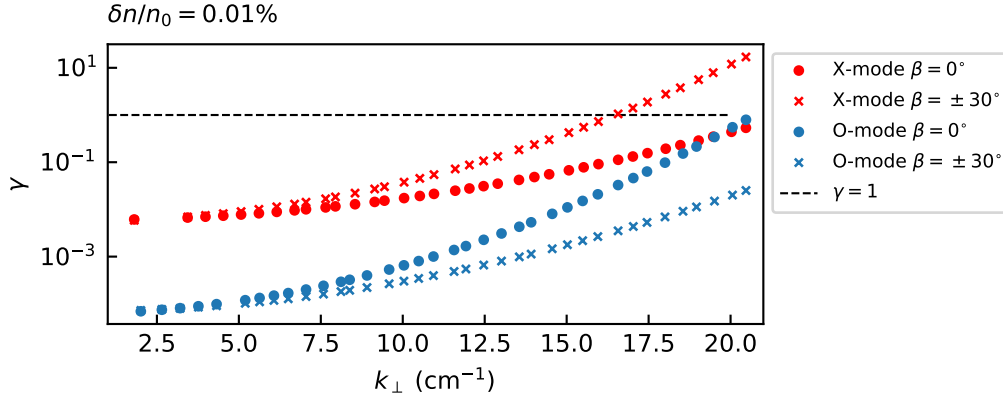
Figure 6.12: Non-linearity factor γ cf. equation (5.7) for $\delta n/n_0 = 0.01\%$ in slab geometry. The Gaussian spectrum with $l_{min} = 0.3\,\text{cm}$ and $l_{max} = 0.6\,\text{cm}$ is used. Varying the tilt angle β leads to a change in the correlation lengths cf. table 6.2. This leads to an increase in γ.

in the non-linearity factor. However, since the turbulence level is in general lowered with respect to the previous sections, γ is not exceeding 1 significantly.

The full-wave results are presented in the fig. 6.13 for O-mode and in fig. 6.14 for X-mode. The non-tilted structure results are shown in blue and red for O-mode and X-mode, respectively. The tilted results are shown in green and purple.

The obtained perpendicular wavenumber spectra are shown on the left. The corrected back-scattered power P_{corr}, regarding the scattering efficiency (see eq. (6.1)) is not applied here to provide better clarity. Due to the tilt, not only the correlation length but also the corresponding turbulent wavenumber is affected. Since Doppler reflectometry is probing in the perpendicular wavenumbers only, a tilt leads to a steepened spectrum. The analytical spectra for $\beta = 0°$ and $\beta = \pm 30°$ cf. (5.20), are shown in black in solid and dashed line-styles.

Both full-wave results for the density wavenumber spectra of the O-mode in fig. 6.13(a) and of the X-mode in fig. 6.14(a) show the mentioned differences in the wavenumber spectra. Nevertheless, they do not agree completely with the analytical spectra. Tilted and non-tilted spectra are less deviated than expected. This can have several reasons, such as the slight non-linearity or the scattering efficiency correction, which was not applied here.
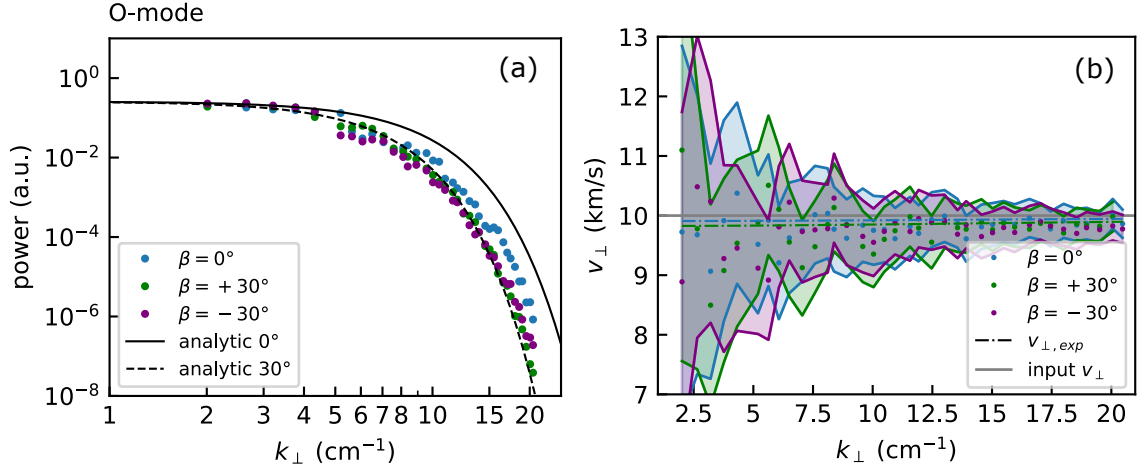
O-mode

Figure 6.13: Full-wave results using O-mode for different tilt angles. The used turbulence pattern are shown in figure 6.11. (a) The density wavenumber spectrum results. The analytic spectra are shown in solid and dashed line-styles. (b) The perpendicular velocities. The full-wave results include an uncertainty band. The expected velocity $v_{\perp,\mathrm{exp}}$ due to the probing beam width in shown in dashed.
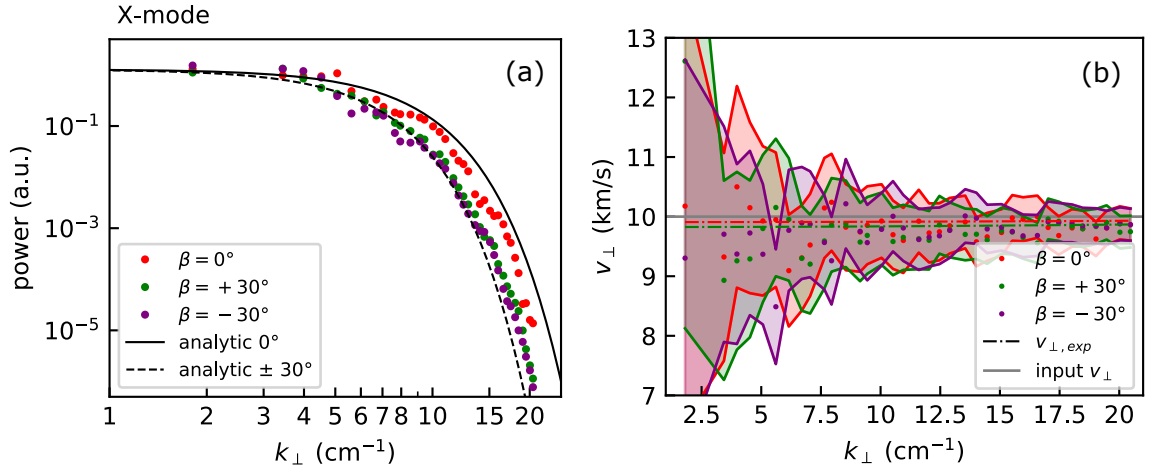
X-mode

Figure 6.14: Full-wave results using X-mode for different tilt angles. The used turbulence pattern are shown in figure 6.11. (a) The density wavenumber spectrum results. The analytic spectra are shown in solid and dashed line-styles. (b) The perpendicular velocities. The full-wave results include an uncertainty band. The expected velocity $v_{\perp,\mathrm{exp}}$ due to the probing beam width in shown in dashed.

The perpendicular velocities are shown on the right in fig. 6.13(b) for O-mode and in fig. 6.14(b) for X-mode. The input velocity is shown in gray. The expected velocities due to the probing beam width $v_{\perp,\text{exp}}$ is shown in dashed. Due to the change in the correlation length, which directly affects the scaling factor (5.21) the velocities slightly vary depending on the tilt. Since the simulations are performed in slab geometry, the spectral resolution is fine and the expected deviation is generally small. For both wave polarizations, the full-wave results show good agreement with the expected deviations.

Neither between the tilted and non-tilted structures, nor between the different directional tilt angles an additional significant diagnostic effect can be observed.

7 Summary and outlook

7.1 Summary

In the recent past, Doppler reflectometry measurements of the perpendicular propagation velocity of density fluctuations have revealed poloidal asymmetries on various toroidal fusion devices.

This work investigated whether diagnostic effects could explain these observations. For this purpose, both analytical and full-wave simulation approaches were employed.

Analytical investigations showed that the measured perpendicular velocity can be lowered, if the underlying density wavenumber spectrum exhibits spectral decays. The magnitude of the deviation depends on the width of the probing beam and the strength of the spectral decay. An analytical expression could be obtained that can predict these deviations. Note that the application of this analytical approach in experiments can be difficult as for the standard measurement case the wavenumber spectrum is not known.

For the full-wave simulations the code IPF-FD3D, that is developed at the IGVP Stuttgart, was used. The code is based on a finite-difference time-domain method to simulate the propagation and scattering of electromagnetic beams in cold plasma. The full-wave simulations were performed in slab and circular plasma geometry in both O-mode and X-mode wave polarization. The perpendicular propagation velocity of density fluctuations was studied using synthetic turbulence that was generated based on different spectra. Isotropic turbulence was obtained using a white spectrum, a realistic Kolmogorov-like spectrum and a Gaussian spectrum. With the latter, also anisotropic turbulence was generated.

The influence of increasing turbulence levels on the perpendicular velocity measurements was also investigated. In contrast to the measurements of the fluctuation amplitude, which is significantly influenced, no striking dependence can be found for the velocity. Thus, the code IPF-FD3D could validate already existing results from theory and previous full-wave simulations.

Isotropic turbulence was studied in slab and circular geometry. All density wavenumber spectra obtained from full-wave analysis showed an excessive decrease towards higher wavenumbers. This effect could be related to the scattering efficiency and was corrected accordingly. Although the corrected powers gave better agreement with the input spectra, a slight over-correction was observed. This could be due to various assumptions e.g. slab geometry, O-mode probing and linear backscattering in the derivation of the correction factor. Thus, further investigation of the scattering efficiency needs to be performed in the future. The measurement of the perpendicular velocity could validate the analytically predicted discrepancies

for all input spectra. It could be shown that the deviations strongly depend on the underlying turbulence spectrum and on the spectral resolution of the beam. Thus, a significant increase in velocity deviations is observed for curved plasma geometries where the spectral resolution is reduced. Since the frequencies used for probing are directly related to the spectral resolution, the expected and measured velocities vary depending on the polarization of the probing waves. This difference between O- and X-mode probing becomes even more pronounced when a circular geometry is assumed.

Effects on the velocity measurement due to the poloidal variation of the antenna position were studied in circular geometry. Three different antenna positions at the same distance from the poloidal flux surface at which the measurements are made were used. All simulations showed the expected deviation with respect to the input velocity as predicted analytically in the context of this thesis. No other significant deviations were found.

Lastly, anisotropic turbulence, i.e. elongated and tilted turbulence structures, were investigated in slab geometry. Due to the tilt angle of the turbulent structures, a change in the correlation lengths is expected. This has an impact on both the turbulence spectrum and the expected deviation in the velocity based on analytical considerations. The expected difference in the perpendicular density wavenumber spectrum could be reproduced by the full-wave simulations. Also the determined perpendicular velocities showed the mentioned effect.

The investigations presented in this thesis show that there is a diagnostic effect in the perpendicular velocity measurements with Doppler reflectometry. This effect is strongly related to the spectral resolution and thus to the plasma curvature and the probing beam geometry. Furthermore, the effect can lead to apparent poloidal asymmetries when the velocity is measured for different wavenumbers at poloidally different plasma positions. However, these deviations are not of the magnitude observed in the experiments on poloidal asymmetries. Therefore, it can be assumed that they are rather related to the actual behavior of the plasma. Nevertheless, the observed diagnostic effect should be taken into account when analyzing experimental data. Especially in smaller fusion experiments where the spectral resolution is strongly limited, deviations in the measured perpendicular velocity of the density fluctuations are to be expected.

7.2 Outlook

Further research regarding the diagnostic response of Doppler reflectometry will require the use of realistic density fluctuations e.g. obtained from gyrokinetic turbulence codes. This turbulence will include realistic combinations of anisotropic, sheared structures in realistic geometries such as the ASDEX Upgrade plasma shape. In addition, gyrokinetic turbulence allows for the consideration of realistic perpendicular velocities, that include a wavenumber dependent phase velocity v_{ph}.

Initial efforts have already been made. Turbulence data is available, as determined by the gyrokinetic turbulence code GENE [26]. This code can perform local
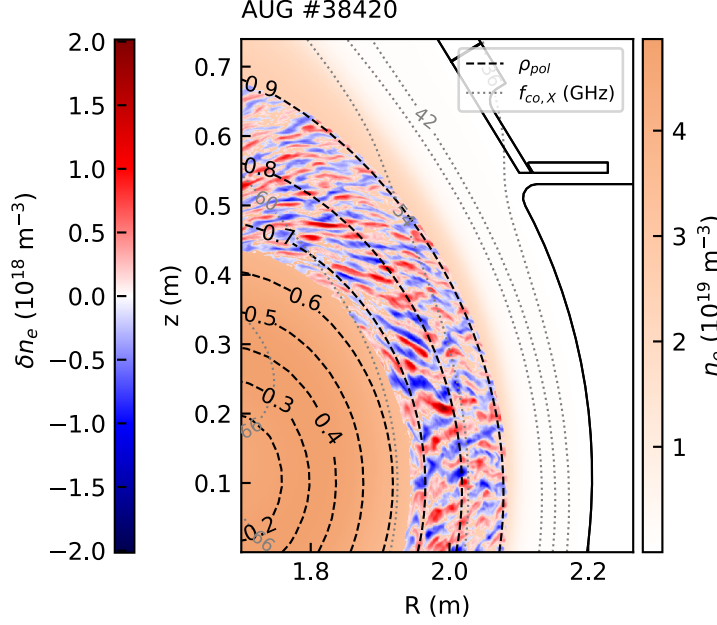
Figure 7.1: Background electron density n_e, ρ_{pol} and the X-mode cut-off frequency $f_{co,X}$ contours in AUG geometry. The n_e fluctuations obtained from GENE are plotted on top for demonstration. The O-mode cut-off layers are not shown since they align with the poloidal flux surfaces.

(flux-tube) and global (full-torus) simulations of turbulence. Here, local simulations on $\rho_{pol} = 0.785$ are used that are based on AUG shot #38420. For this shot, Doppler reflectometry data of the perpendicular propagation velocities of density fluctuations are available, making it suitable for future comparison with the full-wave results. A typical simulation grid , showing the AUG background electron density n_e, the contours of the normalized poloidal plasma radius ρ_{pol} and the X-mode cut-off frequencies $f_{co,X}$ is shown in figure 7.1. The turbulence, that is obtained by GENE is plotted on top for demonstration. The turbulence is clearly anisotropic, including elongated and sheared structures. The turbulence level is much higher than in the synthetic turbulence simulations, such that nonlinear effects in the power response might be evident.

Figures 7.2(a) and 7.2(b) show preliminary full-wave results for the density wavenumber spectrum and the perpendicular velocity measurement, respectively. The results are obtained using O-mode with an antenna located at the outer midplane at $(R, z) = (2.3, 0.1)\,\mathrm{m}$, probing upwards.

The GENE density wavenumber spectrum is shown in orange in fig. 7.2(a). It is the time averaged spectrum from the outer midplane for $k_x = 0$, which is the closest approximation to Doppler reflectometry results [7]. It has two knees where the spectral index changes. One at the main injection range at $k_\perp = 2\,\mathrm{cm}^{-1}$ and one at about $k_\perp = 8\,\mathrm{cm}^{-1}$. The second knee is indicated in the plot by a dotted

7. Summary and outlook
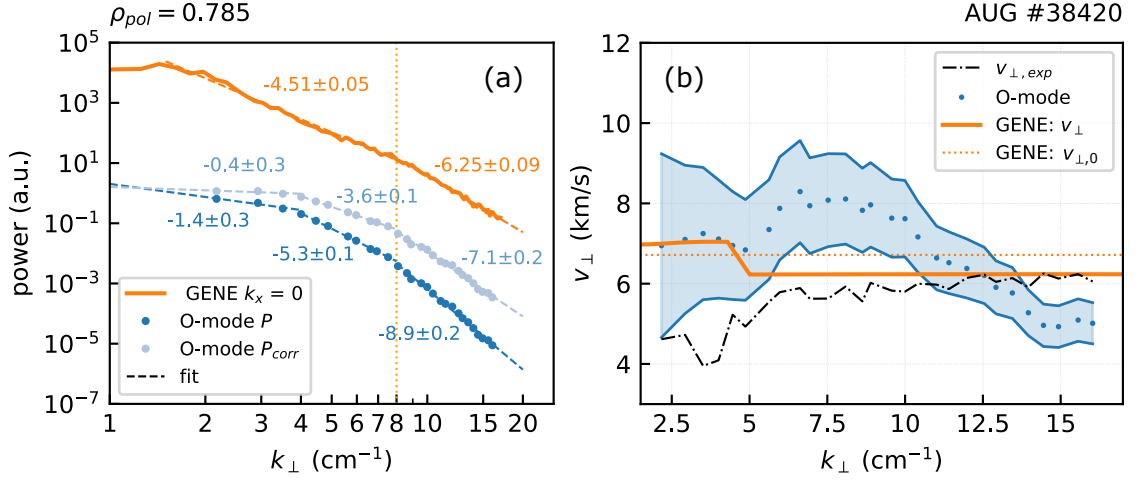
Figure 7.2: Preliminary full-wave results in O-mode polarization (blue), that are measured at $\rho_{pol} = 0.785$ with an antenna located on the outer midplane. (a) The density wavenumber spectrum and (b) the obtained perpendicular velocity are compared with the GENE characteristics (orange) and the expected velocity $v_{\perp,\mathrm{exp}}$ (black) that is obtained analytically.

orange line. The full-wave results are shown in blue. Results using the scattering efficiency cf. (6.1) are indicated in light-blue. Fore the corresponding fits, two knees at $k_\perp = 4\,\mathrm{cm}^{-1}$ and $k_\perp = 8\,\mathrm{cm}^{-1}$ are used.

Due to the high turbulence level of approx. 5%, a significantly increased non-linearity factor $\gamma \gg 1$ is to be expected. Correspondingly, the obtained wavenumber spectrum does not completely agree with the GENE spectrum due to non-linear effects. Neither for the uncorrected nor the corrected full-wave results perfect agreement is observed. This strongly suggests that full-wave simulations are needed as a connecting element for future comparisons of experimental Doppler reflectometer data with GENE.

The results for the perpendicular velocity are shown in figure 7.2(b). The velocity of GENE is shown in orange. The dotted line corresponds to the constant background velocity $v_{\perp,0} \approx 6.8\,\mathrm{km/s}$ that is induced by a toroidal velocity via the poloidal magnetic field in the simulations. The solid line includes also the phase velocity, that is determined by linear simulations. The sign of the phase velocity is related to the dominant underlying micro-instability. A positive sign corresponds to the ion diamagnetic drift direction (ITG modes), while a negative sign indicates propagation in the electron-diamagnetic drift direction (TEM, ETG modes). The expected velocity due to the probing beam width $v_{\perp,\mathrm{exp}}$ is shown in dashed black. It is computed numerically by direct convolution using the GENE spectrum in figure 7.2(a). Due to the diagnostic effect, the slight decrease of the phase velocity is even more blurred. Consequently, the detection of the jump at $k_\perp = 5\,\mathrm{cm}^{-1}$ can be much more difficult in the experiment.

The result from full-wave simulations are shown in blue, including an uncer-

tainty band. Particularly striking is the decay in the velocity for higher wavenumbers, which is unexpected and still needs further analysis. For small wavenumbers $k_\perp < 8\,\mathrm{cm}^{-1}$ an increase in the velocity can be observed that might be connected to the increase in $v_{\perp,\mathrm{exp}}$. A correlation between the decrease in the phase velocity and the full-wave results is not seen. However, obtaining the phase velocity from linear simulations is only a first step. Its determination from high-frequency GENE write-outs may be required to check for nonlinear deviations in v_{ph}.

Further investigation of the gyrokinetic turbulence is necessary and left for future work. For comparison with the experimental measurement data, full-wave data obtained at the same antenna position and with the same frequencies and angles as in the experiment are still needed in particular.

Bibliography

[1] M. Barbarino, Nature Physics **16**, 890 (2020).

[2] J. D. Lawson, Proceedings of the Physical Society B **70**, 6 (1957).

[3] A. Herrmann and O. Gruber, Fusion Science and Technology **44**, 569 (2003).

[4] P. Manz, Turbulence in neutral fluids and plasmas, Lecture Notes (Technische Universität München), 2019/20.

[5] K. Höfler, Master's thesis, Technische Universität München, 2018.

[6] C. Lechte, G. D. Conway, T. Görler, and C. T.-S. and, Plasma Physics and Controlled Fusion **59**, 075006 (2017).

[7] T. Happel *et al.*, Plasma Physics and Controlled Fusion **59**, 054009 (2017).

[8] A. Krämer-Flecken and S. Zoletnik, 39th EPS Conference 2012, 16th Int. Congress on Plasma Physics **36F**, (2012).

[9] L. Vermare *et al.*, Physics of Plasmas **25**, 020704 (2018).

[10] T. Estrada *et al.*, Nuclear Fusion **59**, 076021 (2019).

[11] K. Höfler *et al.*, Plasma Physics and Controlled Fusion **63**, 035020 (2021).

[12] A. Kolmogorov, Akademiia Nauk SSSR Doklady **30**, 301 (1941).

[13] R. H. Kraichnan, The Physics of Fluids **10**, 1417 (1967).

[14] T. Happel, Ph.D. thesis, Universidad Carlos III de Madrid, 2010.

[15] F. Wagner *et al.*, Phys. Rev. Lett. **49**, 1408 (1982).

[16] H. Biglari, P. H. Diamond, and P. W. Terry, Physics of Fluids B: Plasma Physics **2**, 1 (1990).

[17] P. H. Diamond and Y. Kim, Physics of Fluids B: Plasma Physics **3**, 1626 (1991).

[18] P. Manz, M. Ramisch, and U. Stroth, Phys. Rev. Lett. **103**, 165004 (2009).

[19] G. D. Conway *et al.*, Plasma Physics and Controlled Fusion **46**, 951 (2004).

[20] G. D. Conway, E. Poli, T. Happel, and ASDEX Upgrade Team, Plasma and Fusion Research **5**, S2005 (2010).

Bibliography

[21] M. Hirsch *et al.*, Plasma Physics and Controlled Fusion **43**, 1641 (2001).

[22] Y. Lin, R. Nazikian, J. H. Irby, and E. S. Marmar, Plasma Physics and Controlled Fusion **43**, L1 (2000).

[23] V. V. Bulanin and M. V. Yafanov, Plasma Physics Reports **32**, 47 (2006).

[24] H. Hartfuss, T. Geist, and M. Hirsch, Plasma Physics and Controlled Fusion **39**, 1693 (1999).

[25] J. R. P. Acosta, Ph.D. thesis, Technische Universität München, 2018.

[26] F. Jenko, W. Dorland, M. Kotschenreuther, and B. N. Rogers, Physics of Plasmas **7**, 1904 (2000).

[27] M. Born, Zeitschrift für Physik **38**, 803 (1926).

[28] A. D. Piliya and A. Y. Popov, Plasma Physics and Controlled Fusion **44**, 467 (2002).

[29] I. H. Hutchinson, Plasma Physics and Controlled Fusion **34**, 1225 (1992).

[30] E. Z. Gusakov and A. Y. Popov, Plasma Physics and Controlled Fusion **44**, 2327 (2002).

[31] P. Beckmann and A. Spizzichino, *The scattering of electromagnetic waves from rough surfaces* (International series of monographs on electromagnetic waves, Pergamon Press, Oxford, UK, 1963).

[32] J. R. Pinzón *et al.*, Plasma Physics and Controlled Fusion **59**, 035005 (2017).

[33] C. Lechte, IEEE Transactions on Plasma Science **37**, 1099 (2009).

[34] K. Yee, IEEE Transactions on Antennas and Propagation **14**, 302 (1966).

[35] E. Blanco and T. Estrada, Plasma Physics and Controlled Fusion **50**, 095011 (2008).

[36] E. Poli, A. Peeters, and G. Pereverzev, Computer Physics Communications **136**, 90 (2001).

[37] E. Z. Gusakov, A. V. Surkov, and A. Y. Popov, Plasma Physics and Controlled Fusion **47**, 959 (2005).

Acknowledgments

At this point, I would like to express my sincere gratitude to everyone who supported me during my master thesis.

First and foremost, I would like to thank my supervisors at the IPP.

I thank *Klara Höfler* for all the support and time. Despite the difficulties during the pandemic times, there was always a lively contact and I could always count on her help with any kind of problem.

Another thanks goes to *Dr. Tim Happel* for all the nice meetings where I could always take home new knowledge.

Many thanks to both of them for the always friendly and constructive feedback, which helped me a lot to improve my work.

I further thank *Prof. Dr. Ulrich Stroth* for initiating this master thesis at the IPP. I am very grateful that I had the opportunity to get this insight into research. I would also like to thank for making the trip to Stuttgart and the participation in the DPG meeting possible.

I thank *Dr. Carsten Lechte* for providing the code IPF-FD3D. I had a really nice stay in Stuttgart. Thank you very much for the time and help in learning the code and further scientific support.

I thank *Dr. Tobias Görler*, for providing the data from GENE. I appreciate all the suggestions and kind explanations.

I thank all these people for their interest in my work and their motivating support in my future plans. I thank everyone who patiently proofread my master thesis. This made my work even better and I learned a lot.

Last but not least, I would like to thank my family and friends who supported me during my studies.